POLITECNICO
MILANO 1863

RE.PUBLIC@POLIMI
Research Publications at Politecnico di Milano

**Post-Print**

This is the accepted version of:

F. Fusi, P.M. Congedo, A. Guardone, G. Quaranta
*Assessment of Robust Optimization for Design of Rotorcraft Airfoils in Forward Flight*
Aerospace Science and Technology, In press - Published online 17/11/2020
doi:10.1016/j.ast.2020.106355

The final publication is available at https://doi.org/10.1016/j.ast.2020.106355

Access to the published version may require subscription.

**When citing this work, cite the original published paper.**

© 2020. This manuscript version is made available under the CC-BY-NC-ND 4.0 license
http://creativecommons.org/licenses/by-nc-nd/4.0/

Permanent link to this version
http://hdl.handle.net/11311/1152394

# Assessment of robust optimization for design of rotorcraft airfoils in forward flight

F. Fusi[a], P.M. Congedo[b], A. Guardone[a], G. Quaranta[a]

[a] *Department of Aerospace Science and Technology, Politecnico di Milano, Via La Masa 34, 20156 Milano, Italy*
[b] *Team CARDAMOM, INRIA Bordeaux Sud-Ouest, Talence, 33405 Cedex, France*

**Abstract**

The paper compares the deterministic and robust optimization approaches to improve the aerodynamic design of helicopter airfoils. The two formulations are different due to the characteristics of each approach. In the deterministic case, the objective of optimization is the minimization of drag while maintaining a level of lift that guarantees satisfaction of the trimming condition. In the case of robust design, a range of angles of attack and not a single trim condition is considered. Thus, the robust optimization takes the lift-to-drag ratio as a measure of the performance of the airfoil, imposing at the same time an inequality constraint on the lift coefficient to guarantee a sufficient level of lift, and then checking after optimization that the trimming condition can be satisfied. The two approaches are compared showing pros and cons of the robust framework. In general, the robust approach shows the capability to reach the same mean performance of the deterministic one, but with a lower degradation of performance in other conditions considered through the uncertainty. On the other hand, the difficulties in imposing the lift trim condition for the robust formulation may lead to results of limited use.

*Keywords:* Airfoil design, unsteady aerodynamics, uncertainty quantification, robust optimization.

## 1. Introduction

Forward flight is one of the most peculiar and complex flow conditions for rotorcraft blades. The flow encountered by the blade is periodically changing over the azimuth angle and the extremes of this cycle are very different from each other [1], see Figure 2. On the retreating side, the angle of attack is typically high, close to stall, and the blade section Mach number is lower, in the subsonic range or even close to the incompressible limit. For this reason, aerodynamic design should take into account the variability of the flow encountered by the blade, as it is highly possible that an improvement in some conditions may cause a deterioration of performance in others [2].

The unsteady flow encountered on a rotorcraft blade affects the prediction of both local aerodynamics along each blade section and the overall performance. A correct simulation of the complex rotor blade environment requires considering simultaneous speed and angle of attack fluctuations of the incoming airflow, compressibility effects, three-dimensionality of the flow, accurate viscous separation modelling and coupling of the aerodynamic loads with the blade dynamics and aeroelasticity. The accurate prediction of rotor loads requires the definition of detailed computational fluid dynamics (CFD) and computational structural dynamics (CSD) models coupled through appropriate procedures [3]. Even with such models the correlation with experiments is often not so good. In a pivotal work, Bhagwat et al. [4] showed that thanks to three-dimensional (3-D) CFD/CSD simulations it is possible to improve the quality of the predicted loads of complex maneuvered flight conditions. However, highly refined grids are necessary together with computationally expensive turbulence models, as shown also in Ref. [5].

Several authors employed 3-D models to perform blade geometry optimization in hover. Le Pape and Baumier [6] used the 3-D models to optimize

the twist, chord, sweep and anhedral distributions, while Sun and Lee [7] also optimized the airfoil shape in the same flow conditions. Many other authors used 3-D detailed models to perform the rotor optimization in in hover, and in few cases in forward flight as well [8–11]. However, the computational cost is very high, and consequently it is hard to combine the complexity with the necessity to obtain good performance under a range of operating conditions, including other relevant conditions, as suggested for any aerodynamic optimization in Ref. [12]. Consequently, many design approaches regarding aerodynamics of blades have tackled the problem by separating the influence of these combined effects. In this framework, it still makes sense to start from the optimization of the blade airfoils at different radii, and then to work on the optimization of other geometrical elements, like planform, adding an additional external optimization loop around the airfoil optimizer [13]. In this paper the analysis will be limited to the first optimization step, and so limited at the level of airfoil optimization. There is a consensus on the correlation between the lift-to-drag $L/D$ ratio of the airfoil and the $L/D$ ratio of the rotor [14, 15], so this could be taken as performance objective together with the maximization of lift coefficient at high angle-of-attacks.

However, even in the case of optimization of airfoils, the selection of operating conditions is not an easy task. In fact, each airfoil during each rotation is subject to a range of angles of attack and Mach numbers due to the combination of the rotational velocity with flight speed (see Figure 1). This is presented in Fig. 2 where the operating conditions of a blade element are shown for different blade section radial positions. It is clear that both the local angle of attack $\alpha$ and the freestream Mach number $M$ undergo a periodic variation over the rotation period.

To take into account the variation of flow conditions over the azimuth

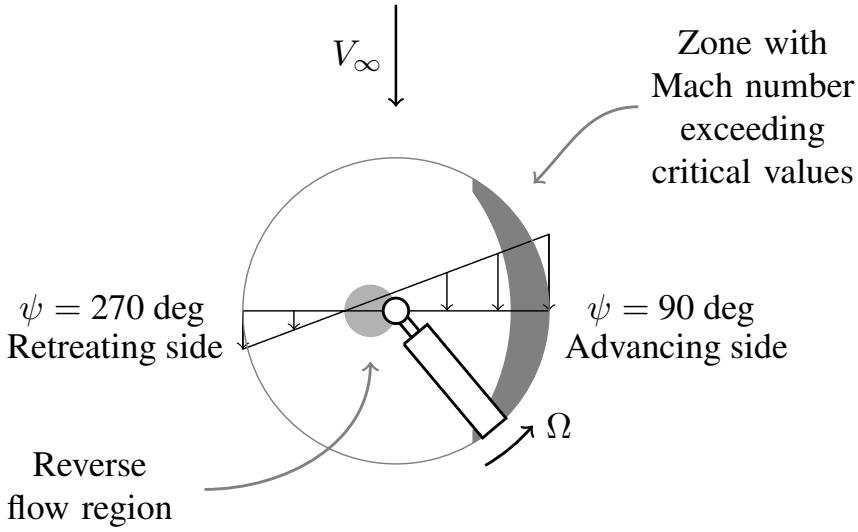


Figure 1: Schematic of distribution of incident speed on a rotor blade in forward flight.

angle, a fully unsteady optimization may be considered, by inserting unsteady models in the optimization loop and directly evaluating the cycle of lift, drag and moment coefficients for each design, as done in [16]. However, this approach is very expensive from a computational point of view, and the accurate prediction of time-varying aerodynamic loads of pitching and plunging airfoils is still a challenge. In most cases, one can resort to a multi-point approach, where the evaluation of the aerodynamic performance is obtained by means of steady models computed at different azimuth angles $\psi$, see Fig. 1. This is the approach followed in several works on optimization of airfoils for rotorcraft, see Refs. [17, 18].

This approach could be used to account for the variability of $\alpha - M$ along the azimuth, but the $\alpha - M$ set changes as the aircraft flies at a different advance ratio or at a different disk loading. However, the increase of the number of points that compose the objective function may become difficult to manage

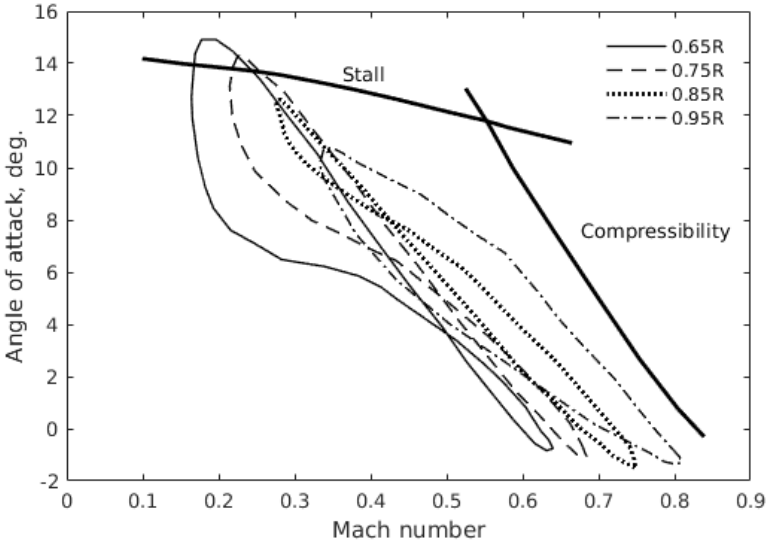


Figure 2: Operating conditions for blade sections (data from Ref. [1, p.296]).

by the optimization task [18], causing problems in the numerical procedures and in the methods to analyse the results. A help in this sense could be achieved by the employment of the robust optimization approach presented in Ref. [19], that allows to look for an airfoil that is minimally sensitive to the variation of operative conditions. This approach is the one pursued here. However, the robust optimization represents a change of paradigm with respect to the deterministic one. Instead of optimizing a single figure of merit or a collection of figures of merit, the robust approach optimizes a statistical measure of the figure of merit or a collection of statistical measures, taking into account the fact that the airfoil will operate in a variable uncertain environment. This change requires a significant modification in the problem formulation.

This work extends the application of robust optimization methods based on the consideration of uncertainties for the optimization of helicopter rotor airfoils, initially presented in Ref. [19] for hover, to the more complex and

challenging case of forward flight. In the following sections, the optimization problem of improving the aerodynamic performance of airfoils is tackled from both deterministic and robust points of view. The robust approach has the potential to lead to airfoils that are more suitable for rotorcraft by taking into account the uncertainty of the operating conditions.

In particular, a two-point optimization problem is set up, considering the two most representative conditions of forward flight: the retreating and advancing blade conditions (see Fig. 1). The idea of using two conditions is aligned with the choice made by other authors dealing with the forward flight optimization, see [17, 18], and allows a thorough comparison of the two optimization approaches presented here. While, the employment of a larger number of blade sections would be conceptually simple, it would only add computational burden to what is presented here.

The optimization will investigate the blade section of the Bo105 rotor [20, 21] used in the full-scale wind tunnel experiments at NASA Ames. The airfoil of the blades used in the test was the NACA 23012. Here the airfoil at the radial station $r/R = 0.85$ is considered and the operating conditions for advancing and retreating sides are taken from the corresponding "figure-of-eight" in the $(M, \alpha)$–plane from Ref. [1] presented in Fig. 2.

The evaluation of the performance of the optimal shapes over the azimuth angle is performed in the post-processing phase with steady models. To motivate the choice of steady models, section 2 discusses the comparison between unsteady CFD predictions and steady computations.

In the deterministic approach presented in section 3, the objective of the optimization is to minimize the drag, whilst maintaining a level of lift that guarantees satisfaction of the trimming condition. In the case of robust design, a single condition is not considered, and the trimming condition cannot

be applied to a range of values for the angle of attack. Thus, the idea is to optimize the lift-to-drag ratio as a measure of performance of the airfoil, impose an inequality constraint on the lift coefficient to guarantee a sufficient level of lift, and then check after optimization that the trimming condition can be satisfied. This approach is used in section 4, and results coming from deterministic and robust optimization are presented and compared in section 5. In both cases only two points over the azimuth angle are considered in the optimization loop, hence a *a posteriori* assessment of the performance is presented in section 6. Finally, conclusions and perspectives are drawn in section 7.

## 2. Unsteady vs steady CFD simulations for the evaluation of loads in forward flight

This section investigates how correct the idea of using steady simulations is for optimization of blade airfoils in forward flight at different azimuth angles, considering that the real flow condition is fully unsteady. The investigation starts with some validation tests, then it presents the simulation of the unsteady loads acting on the reference airfoils, i.e. the NACA 23012 and the NACA 0012 airfoils, during a combined pitching motion and periodic variation of Mach number, representative of the conditions met by rotor airfoils during forward flight.

In the literature, only few works have considered a translation along the freestream direction which is necessary to simulate the speed fluctuation encountered by the blade section [22]. Among these, Refs. [23, 24] have been devoted to the experimental investigation of the effects of coupled oscillations in angle of attack and freestream speed, as it occurs in the real flow around the rotor blade. These studies have tackled conditions below static stall,

for an airfoil undergoing a combination of harmonic pitching, plunging, and fore-aft motion in incompressible flow.

A compressible formulation of the theories presented in Ref. [25] has been developed and assessed in Ref. [26] against a CFD code based on the Euler equations. A numerical analysis of dynamic stall caused by pitching motion and freestream fluctuations has been performed by means of a CFD tool based on the SST $k - \omega$ turbulence model in Ref. [27].

### *2.1. Unsteady CFD set-up and validation*

The simulation is performed using the SU$^2$ software suite [28]. In particular, the unsteady Reynolds-Averaged Navier-Stokes (RANS) equations together with the Spalart–Allmaras model [29] are used to simulate the flowfield around the airfoil. The numerical grid is a C-type, structured mesh (Fig. 3) with 77792 rectangular cells. The number of airfoil wrap-around points is 128, while the normal points are 256. The grid extends $\pm$ 30 chords around a unit chord airfoil (Fig. 3b) and the wall $y^+$ is equal to one, since a wall functions are not used in the simulation. Grid convergence studies are reported in [30].

The time-varying freestream velocity and angle of attack have the following time dependency

$$V(t) = V_\infty \left(1 + \lambda \sin(\omega t)\right) \tag{1}$$

$$\alpha(t) = \alpha_0 + \Delta\alpha \sin(\omega t + \overline{\psi}) \tag{2}$$

where $V_\infty$ is the mean freestream speed, $\lambda$ is the percentage of variation in the freestream speed, $\omega$ is the angular velocity of the fluctuations, $\alpha_0$ is the mean angle of attack, $\Delta\alpha$ is the amplitude of the angle of attack oscillation, and $\overline{\psi}$ is the phase angle. The freestream velocity direction is not modified during pitch oscillations.

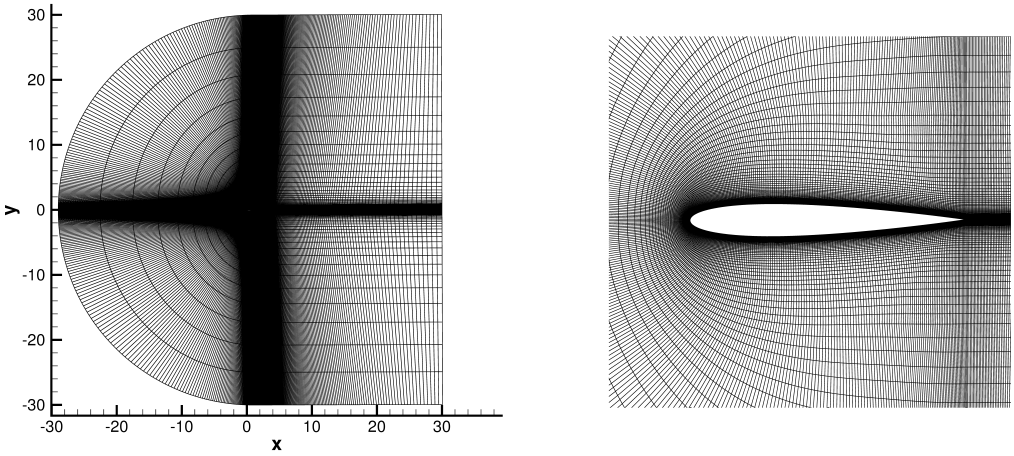


(a) C-mesh.

(b) Close-up on the airfoil.

Figure 3: Typical mesh used for unsteady RANS CFD computations.

To obtain the sinusoidal variation to the freestream velocity of Eq. (1), a time-varying translation of the airfoil along the direction of the mean angle of attack $h(t)$ is performed with the following time dependency

$$h(t) = -\frac{V_\infty \lambda}{\omega} \cos(\omega t). \tag{3}$$

The time-varying translation and pitching are implemented with a volumetric rigid displacement applied to each cell of the mesh in each iteration of physical time. To be consistent with the experimental data, it is necessary to match the reduced frequency $k = \omega c / 2V_\infty$, where $c$ is the airfoil chord.

The CFD setting is validated against experimental measurements and other computations. Different test cases are considered for the validation. Here, the focus is on the experimental data taken from Ref. [23] for the case of the NACA 0012 airfoil undergoing the speed fluctuation in Eq. (1). The corresponding operating conditions are reported in Tab. 1. The computations have been performed considering 100 intervals for each period $T = 2\pi/\omega$, and 800 dual-time iteration. The number of steps in dual time are set

| $\alpha_0$ [deg] | $\Delta\alpha$ [deg] | $V_\infty$ [m/s] | $Re$ | $M_\infty$ | $\lambda$ | $k$ | $\overline{\psi}$ [deg] |
|---|---|---|---|---|---|---|---|
| 6. | 0. | 25 | $4{\cdot}10^5$ | 0.07 | 0.114 | 0.101 | 0 |

Table 1: Operating conditions for validation of SU2 model of NACA0012 airfoil with experimental data from Ref. [23].

to 800 to guarantee that the residuals of the equations are always lower than 1e$^-$4 for every time step. It is noted that the simulation with time-varying freestream Mach number requires a streamwise translation of the airfoil with amplitudes depending on the chosen variation of speed, but also on the reduced frequency. In some cases, the amplitude of this motion may exceed 5 chords, therefore it has been found necessary to both reduce the time step — to apply a small translation at each outer iteration — and increase the number of dual time steps — to guarantee accuracy. Figure 4 presents the lift ratio $L/L_{st}$ between the unsteady lift $L$ and the steady value $L_{st}$, i.e. the value computed when both $\lambda$ and $\Delta\alpha$ are equal to zero in Eqs. (1–2), plotted against the azimuth angle $\psi = \omega t$. A very good agreement is found between the CFD result obtained with the SU$^2$ software and the experimental data, with a maximum error affecting the amplitude of the lift ratio by 6%.

Additionally, the numerical data presented in Ref. [26] for the NACA 0006 airfoil oscillating in pitch only has been compared to the results obtained with the unsteady CFD set-up presented in the preceding section. In this case, it was possible to also compare the pitching moment. The resulting aerodynamic coefficients are presented in Fig. 5.

More extensive details on the validation can be found in Ref. [30] where results of combined pitch and freestream velocity oscillations can be found too. As a final remark, it is noted that experimental data for these kinds of oscillating airfoils are scarce, and that measurements of the unsteady drag

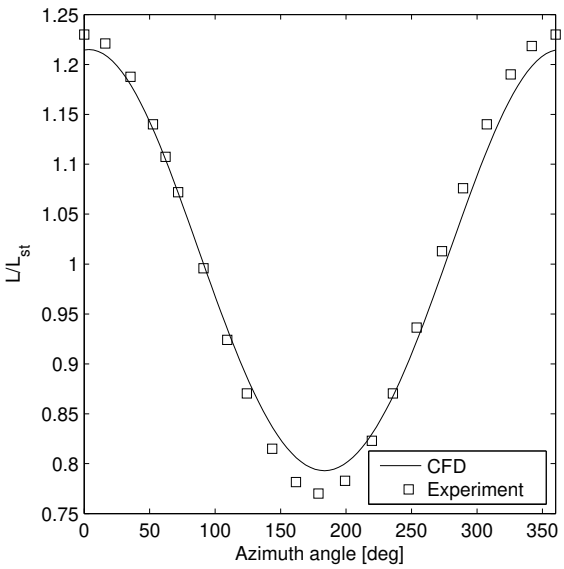


Figure 4: Lift ratio $L/L_{st}$ as a function of the azimuth angle $\psi = \omega t$, for an airfoil undergoing freestream Mach number variation (Eq. (1)). Comparison of experiment(Ref. [23]) vs CFD computation. Maximum error of CFD SU2 model equal to 6%.

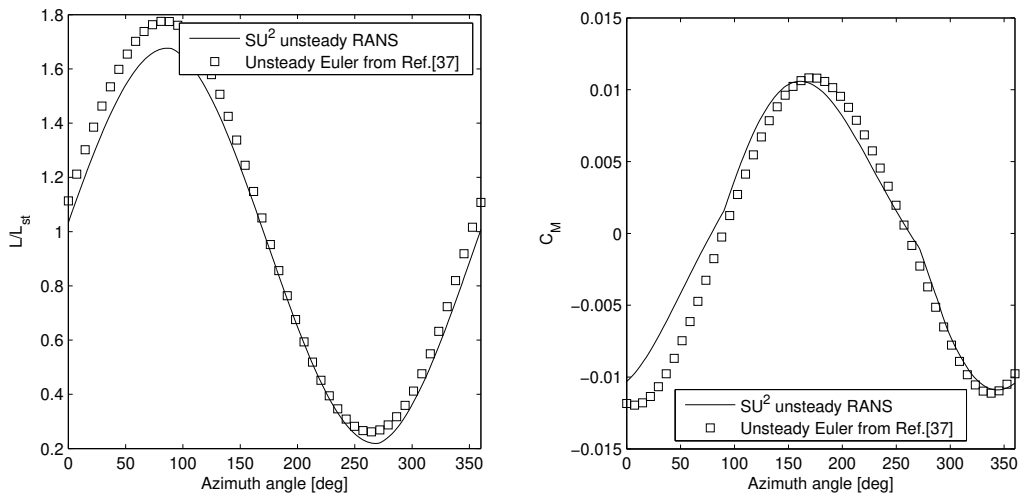


(a) Lift coefficient.

(b) Moment coefficient.

Figure 5: Lift ratio and moment coefficient for a NACA-0006 harmonically pitching airfoil with $\alpha = 2 + 2\sin(\omega t)$ deg, reduced frequency $k = 0.2$.

coefficients are not assessed in the respective literature.

### *2.2. Comparison of steady and unsteady simulation*

The estimate of the lift and drag coefficients obtained with the CFD set-up are compared to the steady approximation used in the optimization problem. This comparison is obtained by computing the aerodynamic coefficients by means of an unsteady RANS simulation presented in the preceding section and different steady models:

- for the advancing side, an Euler simulation with $SU^2$ is performed, with the set-up that will be later presented for the optimization problem (section 3.2). Since the Euler equations are used, a correction associated with viscous effects is added to the inviscid $SU^2$ estimate combining the van Driest II method and a form-factor correction as presented in Ref. [31];
- for the retreating side, the XFOIL solver is adopted
- for the remaining intermediate points, the MSES code is used.

The aerodynamic models used in this optimization problem are different for each side of the blade in order to capture the specific features of the flow in such different operating conditions, while limiting the computational effort.

On the retreating side featuring subsonic conditions below the static stall boundary, XFOIL is considered appropriate, since it is an aerodynamic code that couples panel and integral boundary layer methods for the analysis of subsonic, isolated airfoils [32]. XFOIL provides a fast and sufficiently accurate estimation of the aerodynamic force coefficients for a two-dimensional

section in the range of angle of attack considered in this problem, knowing that the highest value of the angle of attack in the range is below the static stall limit for most airfoils. The transition of the boundary layer is predicted by applying the $e^n$ criterion [33], while compressible effects for low Mach numbers are taken into account by the Karman-Tsien correction [34]. For the adjustable transition parameter $N_{\text{crit}}$ the value of 9 gives satisfactory results for helicopter flows, as shown in Ref. [35].

Instead, for fully developed transonic conditions, such as the one experienced on the advancing side, a solver based on Euler equation, as $SU^2$, able to compute the drag rise caused by the appearance of shock wave was considered sufficient to reach the optimization objective of a shock-free or minimum shock airfoil. In this case no boundary layer is modelled since the viscous drag is not considered as part of the objective of the optimization on the advancing side. The grids used in Euler computations are O-grids, more simplified than those used for RANS computations shown in Fig. 3. This allows to minimize the computational cost.

To run the full unsteady simulation it is necessary to identify the law of variation of the angle of attack, Mach number, and Reynolds number with the azimuth. This law is based on the varying freestream Mach number and angle of attack plotted in Fig. 2, and can be described by means of the following expressions

$$\begin{aligned} M(t) &= M_\infty \left(1 + \lambda \sin(\Omega t)\right) \\ \alpha(t) &= \alpha_0 + \sum_{i=1}^{n_h} \Delta\alpha_i \sin(i\Omega t + \overline{\psi}_i), \quad n_h = 4 \end{aligned} \tag{4}$$

where $\Omega$ is the blade 1/rev frequency, $M_\infty$ is the freestream Mach number, and $\lambda$ is the percentage variation of Mach number. The angle of attack is described by means of a sine series, where $\alpha_0$ is the mean angle of attack,

$\Delta\alpha_i$ is the angle of attack variation of the $i$-th term in the series and $\overline{\psi}_i$ is the $i$-th phase angle. This structure of the variations has been obtained with a convergence analysis based on a sine Fourier series with increasing number of terms. Figure 6a shows the reference $\alpha - M$ cycle, while Fig. 6b shows the variation of the angle of attack and Mach number with azimuth angle. The values of the variables in Eq. (4) are presented in Tab. 2. They lead to the following extrema used in the optimization loop: (i) a maximum value of the angle of attack equal to 12.5 deg at a Mach number of 0.28 and (ii) a minimum value equal to -1.5 deg at a Mach number equal to 0.75 (see Tab. 4).

For comparison, steady state solutions were computed at eight equidistant azimuth stations starting from azimuth 0 (see Figure 1) for the airfoil at

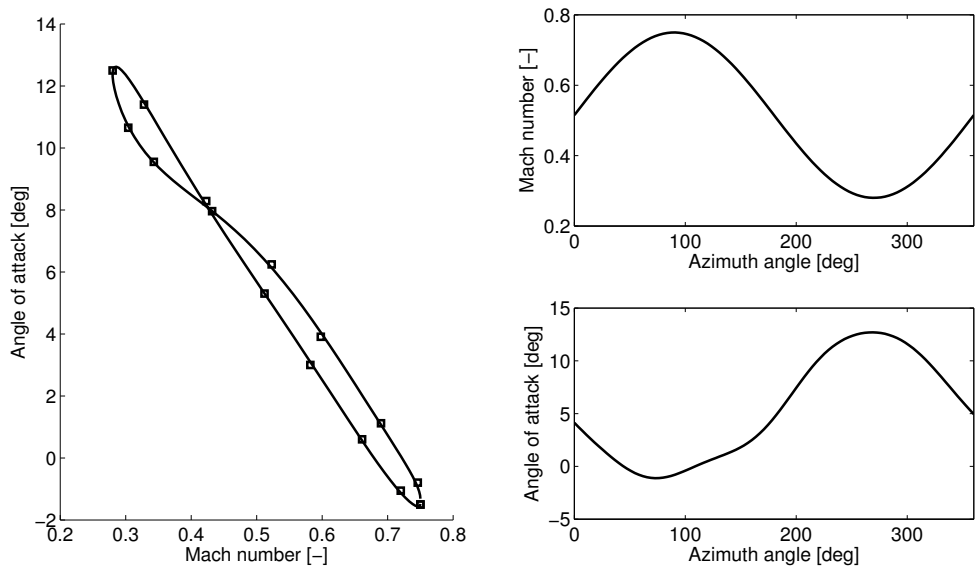


(a) $\alpha - M$: reference cycle (line) and samples from Fourier series approximation in Eq. (4) (squares).

(b) Time varying Mach number (top) and angle of attack (bottom) as function of the azimuth.

Figure 6: Time varying Mach number and angle of attack encountered by airfoils (Eq. (4)).

| $M_\infty$ [-] | $\lambda$ [-] | $\alpha_0$ [deg] | $\Delta\alpha_1$ [deg] | $\phi_1$ [deg] | $\Delta\alpha_2$ [deg] | $\phi_2$ [deg] | $\Delta\alpha_3$ [deg] | $\phi_3$ [deg] | $\Delta\alpha_4$ [deg] | $\phi_4$ [deg] |
|---|---|---|---|---|---|---|---|---|---|---|
| 0.515 | 0.45 | 5.36 | 6.84 | -173.8 | 0.67 | -86.0 | 0.28 | 112.3 | 0.2 | -22.5 |

Table 2: Parameters used in Eq. (4) to impose the variable angle of attack and Mach number to the NACA 0012 and NACA 23012 airfoils.

$r/R = 0.85$.

| | NACA 0012 | | | NACA 23012 | | |
|---|---|---|---|---|---|---|
| | Unsteady | Steady | Diff. | Unsteady | Steady | Diff. |
| $avg(C_L)$ | 0.591 | 0.588 | 0.5% | 0.756 | 0.769 | 1.8% |
| $avg(C_D)$ [counts] | 126.61 | 110.18 | 12% | 121.26 | 101.51 | 16% |

Table 3: Comparison of average drag coefficient and lift coefficient obtained from steady and unsteady computations for NACA 0012 and NACA 23012 airfoils.

The results for the NACA 0012 airfoil and NACA 23012 airfoil are presented in Fig. 7 and Fig. 8, respectively. The average aerodynamic coefficients over the azimuth angle are presented in Tab. 3. Excellent agreement is observed with regard to the lift coefficient, both in terms of average value and amplitude oscillations. The differences between the unsteady CFD-based average and the steady value is less than 1% for the NACA 0012 airfoil and less than 2% for the NACA 23012 airfoil. In terms of drag coefficient, the discrepancy between the unsteady results and the steady approximation is more pronounced. The unsteady wake effects are completely neglected in the steady approximation and they greatly affect the drag coefficient, more so than in the case of the lift coefficient. This is most likely the reason for this reduction in accuracy. Nevertheless, the average values of the drag

coefficient differ by 12% and 16% for the NACA 0012 and NACA 23012, respectively. The magnitude of the error for the steady approximation is encouraging, and the different steady models are considered an acceptable solution to significantly reduce the computational cost of the optimization loop, both deterministic and robust. Additionally, Figs. 7-8 show that,even if locally at certain azimuth angles the difference between steady and unsteady drag coefficients may be significant, the two azimuth angles selected are reasonably representative of the range of drag coefficients met by the airfoil during each revolution. The average drag coefficient per rotor turn that influences the torque can be estimated using the steady state approximation at a fraction of cost necessary to run a fully unsteady analysis.

The use of this variable fidelity approach allows for an efficient exploitation of computational resources, as pointed out by Ref. [36]. This is especially important for robust optimization that are always computationally intensive [19]. For more details on how this combination of XFOIL, MSES and Euler $SU^2$ has been identified as the best trade off between accuracy and computational cost, the reader is referred to [19]. In addition, the work presented in Ref. [16] backs up this conclusion. In fact, Reference [16] demonstrates that optimal solutions are not greatly affected by the use of either an unsteady or steady model, as long as the reduced frequency is moderate. This is often the case for rotorcraft where 1/rev frequency is typically below a reduced frequency of 0.06 [37, p. 449]. For this specific Bo-105 rotor the 1/rev reduced frequency, related to freestream velocity variation, is equal to 0.034, and the highest reduced frequency reached by angle of attack variation is 0.12 (see Section 6).

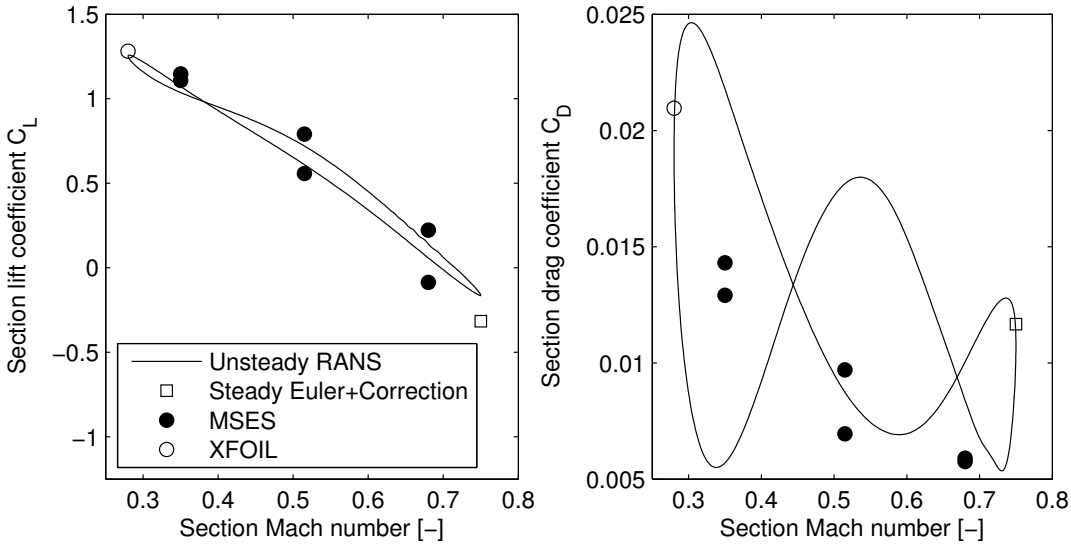


(a) Lift coefficient. (b) Drag coefficient.

Figure 7: Cycle of lift and drag coefficient of the NACA 0012 airfoil.

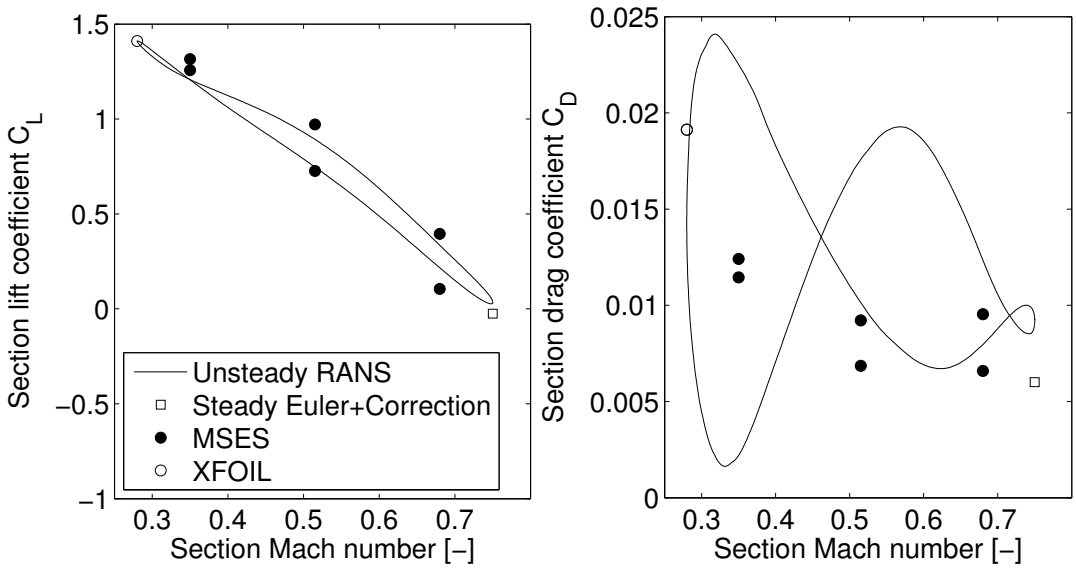


(a) Lift coefficient. (b) Drag coefficient.

Figure 8: Cycle of lift and drag coefficient of the NACA 23012 airfoil.

## 3. Deterministic forward flight optimization

The deterministic optimization of a helicopter rotor airfoil in forward flight typically consists in the minimization of the drag coefficient $C_D$, whilst ensuring the satisfaction of constraints on the lift $C_L$ and moment $C_M$ coefficients. Examples of such an approach are given in Refs. [17, 18, 38]. The constraint on the lift coefficient is set to maintain the trim condition of the entire helicopter.

Here, a target lift coefficient $\overline{C_L}$ is set to consider a specific trim condition, and the moment coefficient is bounded within a given threshold $\overline{C_M}$ to avoid excessive loading on the blade pitch link. The objectives on the advancing and retreating sides are conflicting with one another. In fact, an optimal shape for the advancing side would be a mildly cambered airfoil to postpone drag rise to higher Mach number values, whereas the adoption of a highly-cambered airfoil on the retreating side could be better for higher angle of attack, for instance by means of nose-droop.

In mathematical terms, the two single-objective optimization problems may be formulated as follows

$$\begin{aligned} \text{minimize:} \quad & C_{D_i}(\boldsymbol{x}) \\ \text{subject to:} \quad & C_{L_i}(\boldsymbol{x}) = \overline{C_{L_i}} \qquad |C_{M_i}(\boldsymbol{x})| \leq \overline{C_{M_i}} \\ \text{by changing:} \quad & \boldsymbol{x} \end{aligned} \tag{5}$$

where $\boldsymbol{x}$ are the design variables, and the subscript is related to the advancing or retreating side as shown in Table 6.

The values of the lift constraint $\overline{C_{L_i}}$ are set for each side with the intent of producing a design that improves the performance of the baseline NACA 23012 airfoil. The aerodynamic coefficients of the NACA 23012 airfoil at the specified operating conditions are presented in Tab. 4. Those coeffi-

| Position | Case # | $\alpha$[deg] | $M$[-] | $Re$ [-] | $C_L$ [-] | $C_D$ [counts] | $C_M$ [-] |
|---|---|---|---|---|---|---|---|
| Advancing | 1 | -1.5 | 0.75 | 4.6e6 | -0.025 | 86.97 | 0.02 |
| Retreating | 2 | 12.5 | 0.28 | 1.7e6 | 1.411 | 191.3 | 0.03 |

Table 4: Aerodynamic coefficients of Bo-105 NACA 23012 airfoil at radial station $r/R = 0.85$ on the advancing and retreating sides.

cients are taken from Ref. [39]. It is possible to note that the NACA 23012 airfoil provides a slightly negative lift on the advancing side. At high advance ratio it is possible the outer portion of a helicopter blade can operate at slightly negative lift. However, to avoid any possible confusion it has been chosen to change $\overline{C_{L_1}}$ into a slightly positive value set to generate lift. Furthermore, the constraint on the moment coefficient has been enlarged with respect to the value of the NACA 23012 airfoil to give more freedom to the design optimization and explore design solutions which may have a larger moment coefficient but better performance in the transonic condition.

To complete the scenario of deterministic optimization problem, a single-objective optimization with compromise performance is presented. The optimization problem in this case is defined as follows

$$\begin{aligned} \text{minimize:} \quad & \frac{1}{2}\sum_{i=1}^{2} w_i C_{D_i}(\boldsymbol{x}) \\ \text{subject to:} \quad & C_{L_i}(\boldsymbol{x}) = \overline{C_{L_i}} \qquad |C_{M_i}(\boldsymbol{x})| \leq \overline{C_{M_i}} \quad i = 1, 2 \\ \text{by changing:} \quad & \boldsymbol{x}, \end{aligned} \tag{6}$$

where $w_i$ are weights chosen from the drag coefficient of the optimal airfoils obtained in the single-point optimization cases (see Tab. 5 for values). In this way the each product $w_i C_{D_i}$ will be roughly equal to one. The weights are used to identify the trade-off point between retreating and advancing blade

| Case | $M$[-] | $Re$ [-] | $\overline{C_L}$ | $\overline{C_M}$ | $w_i$ [1/counts] |
|---|---|---|---|---|---|
| 1. | 0.75 | 4.6e6 | 0.025 | 0.08 | 1/2 |
| 2. | 0.28 | 1.7e6 | 1.411 | 0.04 | 1/160 |

Table 5: Operating conditions and aerodynamic constraints for airfoil optimization in the advancing (1.) and retreating (2.) side.

section performance.

### *3.1. Design variables*

Particular attention is drawn to the design variables. To describe an airfoil shape with a finite set of variables, the Class/Shape function Transformation (CST) [40] is used. The parameterization is well-defined by specifying two functions: a geometry class function $C$ and a shape function $S$ that defines the particular shape of the geometry. In this case, the airfoil shape is decomposed into the camber mean line $\zeta_c$ and the normal thickness $\zeta_t$ distributions. The CST is applied to $\zeta_c$ and to $\zeta_t$ of the airfoil and it reads

$$\begin{aligned}\zeta_c(\chi) &= C(\chi)\ S(\chi) + \chi\ \zeta_{TE_c} = C(\chi) \cdot \sum_{i=0}^{n} A_i^c S_{N,i}(\chi) + \chi\ \zeta_{TE_c} \\ \zeta_t(\chi) &= C(\chi)\ S(\chi) + \chi\ \zeta_{TE_t} = C(\chi) \cdot \sum_{i=0}^{n} A_i^t S_{N,i}(\chi)\end{aligned} \tag{7}$$

where $\chi = x/c$ is the non-dimensional chordwise coordinate, the coefficients $A_i^c$, $A_i^t$ define the Bernstein polynomial coefficients of the camber line and thickness distributions respectively, $S_{n,i}$ is the $i$-th term of the Bernstein polynomial of order $N$ [40].

The thickness distribution is taken in perpendicular direction with respect to the camber mean line. Then, the camber line and thickness distribution are such that the upper surface $\zeta_u$ and lower surface $\zeta_l$ are obtained applying

the thickness perpendicular to the camber line, as follows

$$\zeta_u = \zeta_c + \zeta_t \cos(\epsilon)$$
$$\zeta_l = \zeta_c - \zeta_t \cos(\epsilon), \tag{8}$$

where $\epsilon = \arctan\left(\frac{\mathrm{d}\zeta_c}{\mathrm{d}\chi}\right)$. Please note that the $\chi$ coordinate of the resulting airfoil will also be affected by this summation of vectors.

The coordinate of the camber mean line at the trailing edge is set to zero to consider a closed trailing edge and null geomenull In addition, the class functions for the camber line $C_c$ and the thickness distribution $C_t$ are defined as follows

$$C_c(\chi) = \chi(1-\chi) \quad C_t(\chi) = \sqrt{\chi}(1-\chi). \tag{9}$$

While the class function for the thickness distribution is the one suggested in Ref. [40] to define a rounded nose distribution close to the leading edge, the class function for the camber presents a linear term to avoid vertical slope of the camber distribution at the leading edge. In addition, the linear term of the class function permits to directly relate the first coefficient of the shape function $A_0^c$ to the slope of the camber line at the leading edge.

The coefficients of the shape function $S(\chi)$ design variables $\boldsymbol{x}_s$ of the optimization problem. A convergence study, suggested the employment of a 4th order polynomial for each distribution, that yields a total of 10 airfoil design variables plus the angle of attack.

The order of the polynomial could be chosen based on a convergence analysis of the CST. To do this, an extensive numerical campaign has been performed for a representative group of helicopter rotor airfoils — e.g. NACA23012, SC1095, SC1094 — by using an increasing polynomial order, up to 7-th order to obtain complex geometrical features, like the trim tab of the HH02 (for further details see Ref. [19]).

In addition to the coefficients describing the shape of the airfoil, the angle of attack can be regarded as a design variable. In fact, it is possible to solve the constrained optimization problem stated in Eq. (5) by acting on the airfoil design variables $\boldsymbol{x}_s$ to minimize the drag coefficient and on the angle of attack to track the target lift coefficient inside two nested loops. The underlying idea is an analogy with the blade collective pitch control: to increase thrust it is necessary to act on the collective pitch, which changes the angle of attack of the blade section.

Thus, each airfoil tested in the optimization loop is obtained with a specific set $\boldsymbol{x}_s$, and its performance is evaluated by computing the angle of attack $\alpha$ that provides the desired lift coefficient. The nested optimization loops used to implement this procedure are described in detail in Section 3.3. Thus, the resulting set of design variables is $\boldsymbol{x} = \{\boldsymbol{x}_s, \alpha\}$.

### *3.2. Aerodynamic models*

The models used to describe the aerodynamic loads on the airfoil on the advancing and retreating sides were described in section 2.2.

For the computation inside the optimization loop with SU$^2$, a two-dimensional coarse structured mesh of 20480 rectangular cells is used (see Fig. 9). The mesh extends to $\pm 25$ chords around the airfoil. For each airfoil in the optimization loop, the computation runs for 500 iterations starting from a baseline solution of the NACA0012 airfoil. The mesh is deformed by displacing the airfoil boundary cells according to the new geometry and by translating the displacement to the volume cells with a method based on the finite element method discretization of the linear elasticity equations [28]. The element stiffness is set inversely proportional to the wall distance, and 500 smoothing iterations are applied to get a regularly deformed mesh.

The computational cost for each steady evaluation of the figure of merit

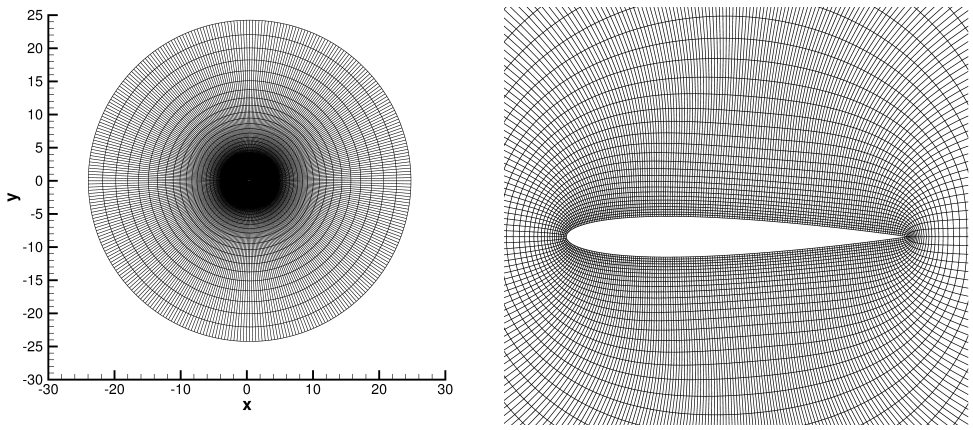


(a) O-mesh. (b) Zoom.

Figure 9: Coarse structured grid around NACA-0012 (20480 cells) for $SU^2$ Euler inviscid computations inside the optimization loop.

using the high fidelity Euler model is about fifteen times that of running a solution with the low fidelity XFOIL solver.

### *3.3. Optimization algorithm*

To solve the optimization problem in Eq. (5), a Non-dominated Sorting Genetic Algorithm [41] is chosen for its ability to explore the design space. Evolutionary algorithms have been employed to tackle many engineering optimization problems. Applications to aerodynamic optimization problems can be found for instance in Refs. [42–44]. The main advantages of such approaches are the possibility to tackle multi-objective problems without scalarization and to exhaustively explore the design space. On the other hand, they are very expensive from a computational point of view because they require many computations of the objective function, even in the region of the domain where designs with poorer performance are present. Main tuning parameters of the algorithm are the population size, the number of generations, the crossover and mutation probabilities pc, pm and the so-

called sharing parameter used to take into account the relative isolation of an individual along a dominance front. Typical values for the crossover and mutation probabilities $pc = 0.9$, $pm = 0.1$ are chosen and the sharing parameter is set using a formula based on the number of design variables.

After performing an initial generation of 200 individuals to explore the design space, 40 individuals are then retained and evolved during 30 generations.

Inside the genetic algorithm loop, an inner loop is nested to deal with the lift coefficient constraint (see Fig. 10). In particular, for each design vector $\boldsymbol{x}_{s,k}$ of the $k$-th iteration in the genetic loop, a secant method is used to find the angle of attack $\overline{\alpha}$ that guarantees $C_{L,k} = \overline{C_L}$. The $i$-th iteration of the secant loop reads

$$\alpha_i = \alpha_{l_i} + \frac{\alpha_{r_i} - \alpha_{l_i}}{C_L(\alpha_{b_i}) - C_L(\alpha_{a_i})} \left(\overline{C_L} - C_L(\alpha_{a_i})\right) \tag{10}$$

where $\alpha_{l_i}$ and $\alpha_{r_i}$ are the left and right boundaries of the interval in which the angle of attack is sought for and they satisfy: $C_L(\alpha_{r_i}) > \overline{C_L}$ and $C_L(\alpha_{l_i}) < \overline{C_L}$. The left and right values are updated according to the value of the lift coefficient for the current $\alpha_i$: if $C_L(\alpha_i) > \overline{C_L} + 0.0005$, then $\alpha_{r_{i+1}} = \alpha_i$; if $C_L(\alpha_i) < \overline{C_L} - 0.0005$, $\alpha_{l_{i+1}} = \alpha_i$, and if $|C_L(\alpha_i) - \overline{C_L}| \leq 0.0005$, the loop breaks.

The method converges in a few iterations, owing to the quasi-linearity of the lift coefficient for most airfoils in the vicinity of considered values of the angle of attack. Lack of convergence within a few iterations is not critical, because this happens for airfoils with poor values of the lift coefficient that should be discarded anyway. The result of the two nested loops is a set of optimal solutions defined by a design vector $\{\boldsymbol{x}_s, \alpha\}$. It is noted that the inner trim loop targets the equality constraint on the lift coefficient, but the resulting design vector atisfy the moment coefficient constraint.

Additionally, a constraint on the minimum allowable airfoil thickness has been considered to obtain airfoils that satisfy also structural requirements. The lower limit for thickness was set at 10%. Airfoils with a thickness below the threshold were simply discarded during the creation of a new generation of individuals.

## 4. Robust optimization problem

The objective of robust optimization is to design an airfoil that is minimally sensitive to the variation of the operating conditions. In this case, it is considered that the operating conditions at which the blade section will operate are affected by the uncertainty arising due to modelling assumptions of physical parameters necessary at the design stage.

Due to the uncertainty, the objective function $f$ is no longer only a function of the design variables $\boldsymbol{x}$, but it also depends on the uncertain variables $\boldsymbol{\xi}$. Within this uncertain framework a minimization with a target lift coefficient at a specific design condition loses its meaning. However, a robustly optimal airfoil with a satisfactory lift-to-drag ratio in a range of conditions could be used to trim the aircraft at a specific lift coefficient, whilst always keeping a low drag coefficient. In addition, if the robustness of the lift-to-drag ratio will translate into the drag coefficient at a specific target lift coefficient, a robust shape would ensure less variability of the required power due to aerodynamic drag.

In particular, for the problem under analysis, the following objectives are defined for each side of the rotor disk.

1. On the advancing side, the rotor blade encounters transonic flow, so airfoils should typically be designed to delay drag divergence to higher Mach numbers [14, 15]. Thus, the lift-to-drag ratio $C_L/C_D$ is the ob-

jective $f_1$ of the optimization: $f_1 = C_L/C_D$, with the constraint of providing a lift coefficient equal to or greater than the value of the baseline airfoil.

2. On the retreating side, the increase of the lift coefficient is typically sought for [14]: for the blade at 270 deg the ratio $C_L^{3/2}/C_D$ is maximized, which is a measure related to the rotor figure of merit [15] and privileges the lift coefficient over the drag coefficient, that is $f_2 = C_L^{3/2}/C_D$.

Finally, the constraints on the moment coefficient and minimum thickness used in the deterministic case are still considered.

In mathematical terms, the resulting optimization problem can be stated as:

$$\begin{aligned} \text{maximize :} \quad & \mu\left(f_i\left(\boldsymbol{x}_s, \boldsymbol{\xi}\right)\right) \\ \text{and minimize :} \quad & \sigma^2\left(f_i\left(\boldsymbol{x}_s, \boldsymbol{\xi}\right)\right) \\ \text{subject to :} \quad & \mathbf{g}\left(\boldsymbol{x}_s, \boldsymbol{\xi}\right) \leq \mathbf{0} \\ \text{by changing :} \quad & \boldsymbol{x}_s, \end{aligned} \tag{11}$$

where the constraints are collected in vector $\mathbf{g}$. The objective functions of Eq. (11) are related to the statistics of the figure of merit $f_i$: the mean value $\mu$ and the variance $\sigma^2$. The design variables in this case are only $\boldsymbol{x}_s$ , while the angle of attack is considered as one of the uncertain parameters in the robust design problem.

Indeed, the angle of attack $\alpha$ and the Mach number $M$ encountered by the two-dimensional section of the blade are considered as uncertain, because they are affected by uncertainty on the modelling of the physical parameters considered in the design stage. Both aerodynamic and structural uncertainties, may affect the value of the angle of attack and Mach number. In particular, the latter may affect the blade dynamic movement and deformation

that in turn change the relative angle and speed of the airfoil with respect to the flow. Following a probabilistic framework, the uncertain variables are modelled as uniformly distributed random variables around a nominal value. The uniform distribution has been chosen after the analysis of reports on experimental measures available for this rotor, like Ref. [21]. From this reports it is possible to have an idea of the experimental uncertainty but not of the probability density function with which this uncertainty is distributed. Consequently, it has been decided to use a uniform distribution to avoid any bias toward any specific value. In any case, it must be stressed that this choice does not affect the validity of the proposed approach. The nominal conditions are reported in Tab. 4 and the uncertainty band is set to 5% for the Mach number and for the angle of attack, again based on the analysis of experimental results [21]. Also in this case the range was taken looking at the variability desumed by available experimental data [21].

The statistics of the performance $f_i$ are computed by means of an uncertainty propagation technique, a method to propagate the uncertainty affecting the operating conditions into the quantity of interest $f$.

### *4.1. Uncertainty quantification*

A probabilistic framework is employed to deal with the uncertain input data. In this context, the stochastic input quantities $\boldsymbol{\xi}$ are treated as independent continuous random variables. The random vector $\boldsymbol{\xi}$, whose dimension is equal to the number of uncertain variables $n_\xi$, belongs to the probability space $(\Omega, \mathcal{F}, P)$, composed of the sample space $\Omega$, the $\sigma$-algebra $\mathcal{F}$ of the subsets of the events, and a probability measure $P$. It essentially maps the samples in $\Omega = [0,1]^{n_\xi}$ into the random outcomes $\boldsymbol{\xi} \in \Xi$, and it is characterized by the probability density function $p_\xi(\boldsymbol{\xi})$. The output of the system is then a stochastic variable, and therefore the performance $E(\mathbf{y}, \boldsymbol{\xi})$, which

is a function of the solution, is a stochastic variable as well. In the robust optimization, procedure the interest is in reconstructing the mean value and the variance of the quantity of interest; in the following, the stochastic output variable is referred to as $u(\mathbf{y}, \boldsymbol{\xi})$, while its deterministic realization is $\tilde{u}_i(\mathbf{y}, \boldsymbol{\xi}_i)$. Let us define the expected value of the stochastic variable $u$ as follows

$$\langle u \rangle = \int_{\Xi} u(\mathbf{y}, \boldsymbol{\xi})\ p_{\xi}(\boldsymbol{\xi})\ \mathrm{d}\xi,$$

with $p_{\xi}(\boldsymbol{\xi}) = \prod_i^{n_\xi} p_{\xi_i}(\xi_i)$ being the joint probability of the independent input variables.Let us define the inner product operator of two stochastic variables $u$ and $v$ with respect to the joint probability (i.e. the covariance for independent $u$ and $v$)

$$\langle u, v \rangle = \int_{\Xi} u(\mathbf{y}, \boldsymbol{\xi}) v(\mathbf{y}, \boldsymbol{\xi})\ p_{\xi}(\boldsymbol{\xi})\ \mathrm{d}\xi.$$

The mean and variance then read

$$\begin{aligned} \mu(u) &= \langle u \rangle \\ \sigma^2(u) &= \langle u, u \rangle - \langle u \rangle^2. \end{aligned} \tag{12}$$

To reconstruct the quantities in Eq. (12), a Polynomial Chaos (PC) expansion method [45] is used. In fact, under specific conditions, a stochastic process can be expressed as a spectral expansion based on suitable orthogonal polynomials, with weights associated to a particular probability density function. The first study in this field is the Wiener process that was later developed in Ref. [45]. The basic idea is to project the variables of the problem onto a stochastic space spanned by a complete set of orthogonal polynomials $\Psi$ that are functions of the random variables $\boldsymbol{\xi}$. For example, variable $u$ has the following spectral representation

$$u\left(\mathbf{y}, \boldsymbol{\xi}\right) = \sum_{k=0}^{\infty} \alpha_k\left(\mathbf{y}\right) \Psi_k\left(\boldsymbol{\xi}\right) \tag{13}$$

where $\Psi_k$ are the PC orthogonal polynomials and $\alpha_k$ the coefficients of the expansion. In practice, the series in Eq. (13) must be truncated to a finite number of terms $N$, which is determined by

$$N + 1 = \frac{(n_\xi + n_o)!}{n_\xi!\ n_o!},$$

where $n_\xi$ is the dimension of the uncertainty vector $\boldsymbol{\xi}$ and $n_o$ is the order of the univariate polynomial expansion $\phi_i(\xi_i)$ from which the multivariate polynomials $\Psi_k(\boldsymbol{\xi})$ are obtained via tensorization, i.e.

$$\Psi_k\left(\boldsymbol{\xi}\right) = \prod_i^{n_\xi} \phi_i(\xi_i).$$

The polynomial basis $\phi_i(\xi_i)$ is chosen according to the Wiener-Askey scheme [45] in order to select orthogonal polynomials with respect to the probability density function $p_\xi(\boldsymbol{\xi})$ of the input. In this work, because a uniform distribution is considered, Legendre polynomials are employed. The orthogonality property can be advantageously used to compute the PC coefficients of the expansion $\alpha_k$ in a non-intrusive PC framework; this procedure is called Non-Intrusive Spectral Projection (NISP) [42]. In fact, from the orthogonality property it directly follows that

$$\alpha_k = \frac{\langle u(\mathbf{y}, \boldsymbol{\xi}), \Psi_k(\boldsymbol{\xi})\rangle}{\langle \Psi_k(\boldsymbol{\xi}), \Psi_k(\boldsymbol{\xi})\rangle} \qquad \forall k. \tag{14}$$

The computation of the PC coefficients requires an integration of the polynomials that can be estimated with several approaches, among which quadrature formulae are chosen in this study. As a result, the solution of the deterministic problem is required for each quadrature point. Once the polynomial chaos and the associated $\alpha_k$ coefficients are computed. The mean value and the variance of the stochastic solution $u\left(\mathbf{x}, \boldsymbol{\xi}\right)$ (Eq. (12)) are obtained leveraging the orthogonality of the polynomials $\Psi_k$ with respect to the probability

function $p_\xi$:

$$\mu(u)|_{PC} = \left\langle \sum_{k=0}^{N} \alpha_k(\mathbf{y})\,\Psi_k(\boldsymbol{\xi}) \right\rangle = \alpha_0(\mathbf{y})$$

$$\sigma^2(u)|_{PC} = \left\langle \left( \sum_{k=0}^{N} \alpha_k(\mathbf{y})\,\Psi_k(\boldsymbol{\xi}) \right)^2 \right\rangle - \alpha_0^2(\mathbf{y})$$

$$= \sum_{k=1}^{N} \alpha_k^2(\mathbf{y}) \left\langle \Psi_k^2 \right\rangle . \tag{15}$$

Because a uniform distribution is considered also in the forward flight case, Legendre polynomials are employed in the PC expansion. The order of the expansion is retained from a convergence analysis which proved that a fourth-order polynomial is sufficient to accurately capture the statistics. The reconstruction of the statistics is based on the evaluation of the exact function for a set of samples $\boldsymbol{\xi}_k$ in the uncertain variables domain for each design vector $\overline{\boldsymbol{x}_s}$.

## 5. Results

As presented in the previous sections, different optimization problems are performed. A summary of the optimization cases studied in this work is given in Tab. 6. Letters DO and RO stand for the deterministic and robust optimizations, while numbers 1 and 2 refer to advancing and retreating sides, respectively. The case DO0 represents the best trade off airfoil when considering both retreating and advancing sides.

### *5.1. Deterministic optimization*

The results of the deterministic optimization problems are: (i) airfoil DA1 with the optimal drag coefficient on the advancing side, (ii) airfoil DA2 with the optimal drag coefficient on the retreating side, and (iii) airfoil DA0 with

| Case | Objective | Equality constraints | Inequality constraints | Design variables |
|---|---|---|---|---|
| DO1 | $\min C_{D,1}$ | $C_{L_1} = \overline{C_{L_1}}$ | $\lvert C_{M_1}\rvert \leq \overline{C_{M_2}}$ | $\boldsymbol{x}_s, \alpha$ |
| DO2 | $\min C_{D,2}$ | $C_{L_2} = \overline{C_{L_2}}$ | $\lvert C_{M_2}\rvert \leq \overline{C_{M_2}}$ | $\boldsymbol{x}_s, \alpha$ |
| DO0 | $\min \sum_{i=1}^{2} w_i C_{D,i}$ | $C_{L_1} = \overline{C_{L_1}}$ | $\lvert C_{M_1}\rvert \leq \overline{C_{M_1}}$ | $\boldsymbol{x}_s, \alpha$ |
| | | $C_{L_2} = \overline{C_{L_2}}$ | $\lvert C_{M_2}\rvert \leq \overline{C_{M_2}}$ | |
| RO1 | $\max \mu(f_1)$ and $\min(\sigma^2(f_1)$ | | $\lvert C_{M_1}\rvert \leq \overline{C_{M_1}}$ | $\boldsymbol{x}_s$ |
| RO2 | $\max \mu(f_2)$ and $\min \sigma^2(f_2)$ | | $\lvert C_{M_2}\rvert \leq \overline{C_{M_2}}$ | $\boldsymbol{x}_s$ |

Table 6: Summary of optimization problems.

the optimal weighted sum of drag coefficients. These airfoils are presented in Fig. 11 and the characteristics of their geometry are reported in Tab. 7. It is possible to note that the optimal airfoil for the retreating side is highly cambered to cope with the higher angle of attack and it has a lower thickness-to-chord ratio to reduce the drag coefficient. The optimal airfoil for the advancing side generates positive lift owing to a slight camber and greater thickness. The slope of the camber line at the leading edge is controlled by the first coefficient of the parameterization thanks to the modification of the CST discussed in Section 3.1. Both in the overall airfoil geometry and in each specific parameter presented in Tab. 7, it is possible to note that airfoil DA0 represents a trade-off solution between DA1 and DA2, although it appears more similar to the DA1 airfoil. This similarity is likely to be due to the choice of the weighting function.

With regard to performance, the drag coefficients of the optimal airfoils are presented in Tab. 8. The drag coefficient are expressed in drag counts, where one drag count is equal to 0.0001. The gains with respect to the base-

| | DA1 | DA2 | DA0 |
|---|---|---|---|
| Maximum thickness | 0.1187 | 0.1049 | 0.1161 |
| Position of maximum thickness | 0.36 | 0.22 | 0.31 |
| Maximum camber | 0.0054 | 0.0303 | 0.0079 |
| Position of max camber | 0.81 | 0.31 | 0.73 |
| First design variable ($A_0^c$) | 0.065 | 0.289 | 0.107 |
| Camber slope at LE [deg] | 3.704 | 16.098 | 6.108 |

Table 7: Characteristics of the optimal airfoils (for unit chord).

| | $C_{D_1}$ [counts] | $\alpha_1\|_{\overline{C_{L_1}}}$ [deg] | $C_{M_1}$ [-] | $C_{D_2}$ [counts] | $\alpha_2\|_{\overline{C_{L_2}}}$ [deg] | $C_{M_2}$ [-] |
|---|---|---|---|---|---|---|
| DA0 | 0.8947 | -1.059 | 0.0463 | 177.8 | 11.1 | -0.0108 |
| DA1 | 0.6927 | -1.002 | 0.0459 | – | – | – |
| DA2 | 191.99 | -3.101 | 0.1047 | 126.0 | 9.27 | -0.0393 |

Table 8: Performance of the optimal airfoils: performance of DA1 in the retreating side is not reported because DA1 airfoil cannot satisfy lift constraint. The values for the baseline airfoil are reported in Tab. 4.

line NACA 23012 airfoil are presented in Tab. 9. The DA1 airfoil and the DA2 airfoil significantly improve the performance of the advancing and retreating sides, respectively. This was expected for a deterministic optimization that starts from a baseline airfoil that has been used extensively on rotorcraft, as for the Bo-105 helicopter, but that was not specifically developed for rotorcraft flow conditions.

Airfoil DA1 is an airfoil which reduces the drag coefficient by smoothing curvature variations of the upper and lower sides, yielding a shock-free flow-

| | Percentage gain side 1 | Percentage gain side 2 | Relative gain side 1 | Relative gain side 2 |
|---|---|---|---|---|
| DA0 | +99% | +7% | 1/97.2 | 1/1.08 |
| DA1 | +99% | – | 1/125 | – |
| DA2 | – | +34% | – | 1/1.52 |

Table 9: Gain of the optimal airfoils with respect to the baseline NACA 23012 airfoil: gain of DA1 in the retreating side and gain of DA2 in the advancing side are not reported because these airfoils do not satisfy respectively the lift and moment constraints.

field (see the Mach number contour in Fig. 12a). However, on the retreating side, the DA1 airfoil cannot satisfy the lift constraint, therefore its drag coefficient is not reported in Tab. 8 and its gain is not present in Tab. 9. On the other side, airfoil DA2 reduces the drag coefficient of the NACA 23012 airfoil by reducing the peak friction coefficient and by postponing boundary layer transition, as presented in Fig. 13a. However, on the advancing side, the performance of such an airfoil is very poor and a strong shock wave is present on the lower side (see Fig. 12b). The trade-off airfoil DO0 has a significant gain on the advancing side, because it is more similar to the DA1 airfoil. As a matter of fact, a shock-free flowfield is obtained with this airfoil (Fig. 12c), whereas on the retreating side, an earlier transition to a turbulent boundary layer is present, leading to a higher friction coefficient (Fig. 13b).

### *5.2. Comparison with robust optimization*

Two different robust optimization problems are performed, the first one for the advancing side (problem RO1) and the second one for the retreating side (RO2). The Pareto front for the case of the advancing side is presented in Fig. 14a where the two objective functions are the mean value and the

| Airfoil | $C_{D,1}\|_{\overline{C_{L_1}}}$ [counts] | $\alpha_1\|_{\overline{C_{L_1}}}$ [deg] | $\mu_{C_{D,1}}$ [counts] | $\sigma^2_{C_{D,1}}$ [counts$^2$] | $(\sigma/\mu)_{C_{D,1}}$ [-] |
|---|---|---|---|---|---|
| DA0 | 0.895 | -1.059 | 5.26 | 65.75 | 1.54 |
| DA1 | 0.693 | -1.002 | 2.16 | 11.12 | 1.54 |
| RA1 | 0.898 | -1.510 | 2.03 | 5.668 | 1.17 |

Table 10: Drag coefficient of the deterministic airfoil minimizing $C_{D_1}$ (DA1), the trade-off airfoil (DA0) and the airfoil selected from the robust front in the advancing side (RA1).

variance of the lift-to-drag ratio. Please note that in the figure the mean value and the variance are obtained with a scaling factor of 1/10 acting on $f_1 = C_L/C_D$. The reason for this choice is due to the small values of $C_D$ caused by the inviscid approximation combined with shock-free optimal airfoils. The front presents a very robust solution that, however, comes at the expense of poor performance. In the higher part of the front, solutions with high mean value are found.

To compare the results obtained from the Pareto front in RO1 and the deterministic result DA1, a solution or a group of solutions from the front in Fig. 14a should be selected. To do this, the target lift coefficient $\overline{C_{L_1}}$ is compared to the lift coefficients obtained in the samples used for the reconstruction of the mean value and variance in the UQ loop. The lift coefficients for the solutions of the front are plotted in Fig. 14b. From this set, airfoil RA1 is selected, which is the airfoil that exhibits a lift coefficient equal to the target value inside the uncertainty range considered and a high mean value of the lift-to-drag ratio. Airfoil RA1 is also highlighted in Fig. 14a. The value of the angle of attack for which the lift coefficient of airfoil RA1 is equal to $\overline{C_{L_1}}$ is called $\alpha_1|_{\overline{C_{L_1}}}$ and is equal to -1.51 degrees at the Mach number used for the deterministic optimization DO1. As presented in Tab. 10, at this

| Airfoil | $\mu_{C_{L,1}}$ | $\sigma^2_{C_{L,1}}$ | $(\sigma/\mu)_{C_{L,1}}$ | $\mu_{C_{M,1}}$ | $\sigma^2_{C_{M,1}}$ | $(\sigma/\mu)_{C_{M,1}}$ |
|---|---|---|---|---|---|---|
| DA0 | 0.0257 | 4.52e-05 | 0.26132 | 0.0459 | 9.87e-07 | 0.0217 |
| DA1 | 0.0211 | 4.04e-05 | 0.30151 | 0.0457 | 1.81e-06 | 0.0294 |
| RA1 | 0.0253 | 8.20e-05 | 0.35816 | 0.0688 | 1.47e-06 | 0.0176 |

Table 11: Lift and moment coefficient of the deterministic airfoil minimizing $C_{D_1}$ (DA1), the trade-off airfoil (DA0) and the airfoil selected from the robust front in the advancing side (RA1).

condition the performance of the RA1 airfoil is similar to that of the other two optimized in a deterministic way, DA1 and DA0. In fact, the RA1 airfoil too does not present an extended region of supersonic flow and shock waves (see Fig. 15). However, if an uncertainty band is considered around the condition ensuring trim requirement, both the mean value and the variance of the drag coefficient for airfoil RA1 are smaller than the values of airfoil DA1 (see Tab. 10). The table also presents the coefficient of variation, defined as the ratio of the standard deviation $\sigma$ to the mean value $\mu$, to appreciate the dispersion with respect to the mean value.

To complete the analysis, Table 11 presents the mean value and variance of the lift and moment coefficients for airfoil RA1 and airfoil DA1. In the table, it is interesting to note that the mean value of airfoil RA1 is closer to the target value. Additionally, it is possible to see that the mean values of the drag coefficient, lift coefficient, and moment coefficient are obtained with the fourth-order PC expansion, which has been assessed within a convergence study, not reported here for brevity [30]. Despite the presence of shock waves in this range of conditions, the integral values remain smooth throughout the stochastic space and a fourth-order polynomial provides sufficiently accurate

| Airfoil | $C_{D,2}\|_{\overline{C_{L_2}}}$ [counts] | $\alpha_1\|_{\overline{C_{L_2}}}$ [deg] | $\mu_{C_{D,2}}$ [counts] | $\sigma^2_{C_{D,2}}$ [counts$^2$] | $(\sigma/\mu)_{C_{D,2}}$ [-] |
|---|---|---|---|---|---|
| DA0 | 177.8 | 11.13 | 178.4 | 91.32 | 0.0536 |
| DA2 | 126.0 | 9.27 | 126.2 | 28.40 | 0.0422 |
| RA2 | 148.1 | 10.66 | 148.4 | 33.83 | 0.0392 |

Table 12: Drag coefficient of the deterministic airfoil minimizing $C_{D_2}$ (DA2), the trade-off airfoil (DA0) and the airfoil selected from the robust front in the retreating side (RA2).

estimates of the statistics.

The same analysis can be performed for the Pareto front of the retreating side. Figure 16a presents the optimal set of solutions obtained from the robust optimization. As emerged from the results in [19] for the hovering case and the advancing side, interesting solutions from the front are typically those with high mean performance. A possible criterion for decision making in the post-processing of the front is then the selection of non-dominated solutions with a mean value higher than the value of the reference airfoil. This criterion helps removing the solutions with poor performance, but it still retains solutions with lower variance than the reference result thanks to the quality of the Pareto front.

For this subset of airfoils, the comparison between the robust front and the deterministic airfoil is performed in the same way as presented for the advancing side. Figure 16b shows the lift coefficient of the samples used in RO2 with a mean value higher than the reference value. In this case, every airfoil in the optimal set provides a lift coefficient that is greater than the target value $\overline{C_{L_2}}$. Thus, to select an airfoil from the front for comparison, airfoil RA2 has been chosen as a trade-off between the two objectives.

For this airfoil, an angle of attack equal to 10.66 deg is needed to satisfy

| Airfoil | $\mu_{C_{L,2}}$ | $\sigma^2_{C_{L,2}}$ | $(\sigma/\mu)_{C_{L,2}}$ | $\mu_{C_{M,2}}$ | $\sigma^2_{C_{M,2}}$ | $(\sigma/\mu)_{C_{M,2}}$ |
|---|---|---|---|---|---|---|
| DA0 | 1.3998 | 8.37e-04 | 0.207 | -1.069e-02 | 3.84e-06 | -0.18 |
| DA2 | 1.4113 | 8.67e-04 | 0.021 | -3.924e-02 | 6.51e-07 | -0.02 |
| RA2 | 1.4016 | 6.24e-04 | 0.018 | -1.383e-02 | 7.68e-06 | -0.20 |

Table 13: Lift and moment coefficient of the deterministic airfoil minimizing $C_{D_2}$ (DA2), the trade-off airfoil (DA0) and the airfoil selected from the robust front in the retreating side (RA2).

the trim condition. By applying the same uncertainty range as used in the robust optimization case, it is possible to compute the mean value and the variance of the drag coefficient of RA2. These values are higher with respect to the value computed for airfoil DA2 (see Tab. 12). In fact, the optimal deterministic airfoil has a very low value of drag coefficient because it satisfies the lift constraint at a very low angle of attack (9.27 deg) thanks to the highly cambered mean line. However, airfoil DA2 cannot satisfy the moment coefficient constraint in the uncertainty range. As presented in Fig. 17, the moment coefficient exceeds the threshold value $\overline{C_{M_2}}$. On the contrary, the robust optimization formulation guarantees that the optimal airfoils would not incur moment penalties throughout the uncertainty range (see Tab. 13).

The discrepancy in the performance of airfoils DA2 and RA2 is due to the fact that the lift coefficient of the robust airfoil is significantly greater than the target lift coefficient. Thus, the deterministic optimization and the robust optimization are essentially exploring different regions of the design space, according to the specific objectives. To some extent, a fair comparison between the two methods is meaningful if the two methods share the "same" objectives. This means, for example, that for this specific case the target lift coefficient should be higher for the comparison with the robust

airfoils. Another possibility is to define the nominal condition for the robust case starting from the deterministic results. This would at least ensure the presence of the deterministic airfoil in the robust population (as long as it satisfies the constraints). This last strategy appears more straightforward, and the results of its application are reported in another paper [46].

Finally, it must be noted that both optimal robust solutions RA1 and RA2 show an average value of the moment coefficient that is in the imposed limits but higher than the one of DA0, with a limited variance.

## 6. Verification of design along the full range of azimuth angles

Up to this point, the performance of the optimal airfoils is considered only for the advancing and retreating side conditions. However, the blade section encounters different operating conditions over the period of rotation of the blade and an assessment of the performance over the full range of azimuth angles is appropriate. To do this,

With the laws of Eq. (4) and values of Tab. 2 the baseline NACA 23012 develops the trim loads required. However, for the optimal airfoils, new values of the amplitude of the sine terms describing the angle of attack must be computed, because the target lift coefficient is obtained on both sides at a different angle of attack. In other words, the amplitude of the time-varying angle of attack presented in Fig. 6b must be corrected for each optimal shape. In general, the azimuth variation of the angle of attack is caused by the blade cyclic pitch control, the induced velocity of the rotor, the blade dynamics, and aeroelastic deformations. Thus, as a first approximation, it is possible to associate the 2/rev, 3/rev and 4/rev contributions in Eq. (4) to the nonlinear contributions depending on the aerodynamic effects of vortices, wakes and the blade dynamics. These contributions are essentially a function of the

| | DA0 | DA1 | DA2 | RA1 | RA2 |
|---|---|---|---|---|---|
| $\alpha_0$ [deg] | 5.04 | 5.75 | 3.09 | 5.49 | 4.58 |
| $\Delta\alpha_1$ [deg] | 5.88 | 6.51 | 5.97 | 6.76 | 5.87 |

Table 14: Variables of time-varying angle of attack (Eq. (4)) for optimal shapes.

lift produced by the blade, which remains unchanged for the optimal airfoils. However, the first sine term $\Delta\alpha_1$ (1/rev) is directly related to the cyclic pitch control and can be adjusted to maintain the trim requirement. So, only this term is updated for the optimized airfoils, as shown in Tab. 14.

Using the same procedure as shown in section 2, steady state computations are performed at eight azimuth angle stations. The aerodynamic coefficients for the deterministic optimal airfoils (DA0, DA1, DA2) are presented in Fig. 18. It is possible to note that the cycle of the lift coefficient is similar for the three airfoils owing to the equality constraint on the lift coefficient used in the optimization loop. Please recall that airfoil DA1 is not capable of satisfying the trim constraint in the other design condition considered (i.e. the retreating side).

The average of the drag coefficient over the azimuth angle $avg(C_D)$ is then computed and the results are summarised in Tab. 15. The table also presents the results for the airfoils selected from the robust Pareto front, i.e. airfoil RA1 and airfoil RA2. The associated cycles of the aerodynamic coefficients are presented in Fig. 19. As expected, airfoil DA0 provides the best average drag coefficient over the azimuth angle. The penalty of airfoil DA1 in the other design condition (i.e. the retreating side) is higher than the penalty suffered by airfoil DA2 in the other design conditions. As a result, airfoil DA2 has a better average value. Airfoil RA2 has a small penalty

| Airfoil | DA0 | DA1 | DA2 | RA1 | RA2 |
|---|---|---|---|---|---|
| $avg(C_D)$ [counts] | 98.76 | 122.22 | 105.5 | 118.84 | 107.71 |

Table 15: Average drag coefficient for optimal airfoils in forward flight.

with respect to its deterministic counterpart and it also presents a fairly symmetrical cycle. Airfoil RA1 on the other hand has a better average value than the corresponding deterministic airfoil.

## 7. Conclusions

A methodology for robust optimization has been developed to tackle the problem of designing airfoils in forward flight. Robust optimization requires the coupling of the uncertainty quantification method with the optimization algorithm. This coupling increases the computational demand, especially in aerodynamic applications, where a single function evaluation may be very expensive.

To obtain comparable results through robust and deterministic optimizations it has been necessary to consider a fairly different problem set-up.

Deterministic results have proven how different the optimal airfoils are for the advancing and retreating sides. Comparison with the robust approach have shown similarities and differences between the use of the drag coefficient as a deterministic objective and the employment of the lift-to-drag ratio in a robust context. In general, the robust approach has shown the capability to define airfoils that have a mean performance close to the one obtained through a deterministic approach. At the same time, the choice of low variance airfoils though the application of the robust approach ensures the possibility to obtain airfoils that perform adequately without violating the constraints also at other design condition. This is a characteristic that

should be considered fairly important when designing airfoils for rotorcraft, where a significant variability of the operating conditions could be expected.

The identification of the optimal airfoil directly through a robust formulation as the one proposed here, may result cumbersome, given the difficulty in the identification of an optimal airfoil with an uncertainty band across the required lift coefficient. So, a sequential strategy that considers first the application of the deterministic optimization, and then that of the robust optimization should be considered the best approach. Starting from the optimal deterministic airfoils this methodology will lead to airfoils with good performance that suffer of a limited degradation in other design conditions.

Finally, it has been shown that the employment of robust optimization leads to airfoils that have slightly better performance when analyzed for a spectrum of azimuth points wider than those used for optimization. The optimization shown in the paper is based on the adoption of steady state aerodynamic models. In section 2 it has been shown that in the range of reduced frequency considered the adoption of a steady state formulation leads to substantially correct results, even thought unsteadiness may have a significant impact on the overall airfoil drag. So even better results may be expected by a full unsteady robust optimization of airfoils. The adoption of full unsteady models for the evaluation of the objective function does not pose any theoretical difficulty other then a significant increment of computational resources.

## References


[1] W. Johnson, Rotorcraft Aeromechanics, Cambridge University Press, New York, 2013.

[2] M. Drela, Pros and cons of airfoil optimization, in: D. Caughey, M. Hafez

(Eds.), Frontiers of Computational Fluid Dynamics, World Scientific Publishing, 1998, pp. 363–382.

[3] A. Datta, I. Chopra, Prediction of the UH-60A Main Rotor Structural Loads Using Computational Fluid Dynamics/Comprehensive Analysis Coupling, Journal of the American Helicopter Society 53 (4) (2008) 351. doi:10.4050/JAHS.53.351.

[4] M. Bhagwat, H. Ormiston, R.and Saberi, H. Xin, Application of computational fluid dynamics/computational structural dynamics coupling for analysis of rotorcraft airloads and blade loads in maneuvering flight, Journal of the American Helicopter Society 57 (3).

[5] A. Antoniadis, D. Drikakis, G. Zhong, B.and Barakos, R. Steijl, M. Biava, L. Vigevano, A. Brocklehurst, O. Boelens, M. Dietz, M. Embacher, W. Khier, Assessment of cfd methods against experimental ow measurements for helicopter flows, Aerospace Science and Technology 19 (1) (2012) 86–100.

[6] A. Le Pape, P. Baumier, Numerical optimization of helicopter rotor aerodynamic performance in hover, Aerospace Science and Technology 9 (3) (2005) 191–201.

[7] H. Sun, S. Lee, Response surface approach to aerodynamic optimization design for helicopter rotor blade, International Journal for Numerical Methods in Engineering 64 (2005) 125–142.

[8] C. A. Tatossian, S. K. Nadarajah, P. Castonguay, Aerodynamic shape optimization of hovering rotor blades using a non-linear frequency domain approach, Computers and Fluids 51 (1) (2001) 1–15.

[9] H. Farrokhfal, A. R. Pishevar, Aerodynamic shape optimization of hovering rotor blades using a coupled free wake–CFD and adjoint method, Aerospace Science and Technology 1 (2012) 1–10.

[10] K. Collins, L. Sankar, D. Mavris, Application of low- and high-fidelity simulation tools to helicopter rotor blade optimization, Journal of the American Helicopter Society 58 (4) (2013) 1–10.

[11] A. Mishra, K. Mani, D. Mavriplis, J. Sitaraman, Time dependent adjoint-based optimization for coupled fluidstructure problems, Journal of Computational Physics 292 (2015) 253–271. doi:10.1016/j.jcp.2015.03.010.

[12] D. Zingg, S. Elias, Aerodynamic Optimization Under a Range of Operating Conditions, AIAA Journal 44 (11) (2006) 2787–2792. doi:10.2514/1.23658.

[13] N. Vu, J. Lee, Aerodynamic design optimization of helicopter rotor blades including airfoil shape for forward flight, Aerospace Science and Technology 42 (2015) 106 – 117. doi:https://doi.org/10.1016/j.ast.2014.10.020.
URL `http://www.sciencedirect.com/science/article/pii/S1270963815000073`

[14] W. G. Bousman, Airfoil Design and Rotorcraft Performance., in: American Helicopter Society 58th Annual Forum, Montreal, Canada, 2002.

[15] J. G. Leishman, Principles of helicopter aerodynamics, Cambridge University Press, 2006.

[16] S. K. Nadarajah, A. Jameson, Optimum Shape Design for Unsteady

Flows with Time-Accurate Continuous and Discrete Adjoint Method, AIAA Journal 45 (7) (2007) 1478–1491.

[17] D. Fanjoy, W. A. Crossley, Aerodynamic shape design for rotor airfoils via genetic algorithm, Journal of the American Helicopter Society 43 (3) (1998) 263–270.

[18] A. Massaro, E. Benini, Multi-Objective Optimization of Helicopter Airfoils Using Surrogate-Assisted Memetic Algorithms, Journal of Aircraft 49 (2) (2012) 375–383.

[19] F. Fusi, A. Guardone, G. Quaranta, P. M. Congedo, Multi-fidelity physics-based method for robust optimization with application to a hovering rotor airfoil, AIAA Journal 53 (11) (2015) 3448–3465.

[20] R. L. Peterson, Full-scale hingeless rotor performance and loads, TM 110356, NASA (1995).

[21] B. G. van der Wall, 2$^{nd}$ HHC Aeroacoustic Rotor Test (HART II) - Part I: Test Documentation., Braunschweig, Germany, 2003.

[22] D. J. Gosselin, 2d dynamic stall simulations with time-varying freestream representative of helicopter flight, Ph.D. thesis, Ottawa-Carleton Institute for Mechanical & Aerospace Engineering (2014).

[23] D. Favier, A. Agnes, C. Barbi, C. Maresca, A new simulation of airfoil dynamic stall due to velocity and incidence fluctuations, in: 19th AIAA, Fluid Dynamics, Plasma Dynamics and Lasers Conference, American Institute of Aeronautics and Astronautics, 1987.

[24] D. Favier, C. Maresca, C. Barbi, Unsteady aerodynamics of an airfoil in combined translation/pitch oscillations below and through stall, in: 1st

National Fluid Dynamics Conference, American Institute of Aeronautics and Astronautics, 1988.

[25] B. G. van der Wall, J. G. Leishman, On the influence of time-varying flow velocity on unsteady aerodynamics, Journal of The American Helicopter Society 39 (4) (1994) 25 – 36.

[26] A. I. Jose, J. G. Leishman, J. D. Baeder, Unsteady aerodynamic modeling with time-varying free-stream mach numbers, Journal of the American Helicopter Society 51 (4) (2006) 299–318.

[27] K. Gharali, D. A. Johnson, Dynamic stall simulation of a pitching airfoil under unsteady freestream velocity, Journal of Fluids and Structures 42 (2013) 228 – 244.

[28] F. Palacios, , M. R. Colonno, A. C. Aranake, A. Campos, S. R. Copeland, T. D. Economon, A. Lonkar, T. W. Lukaczyk, T. W. R. Taylor, J. J. Alonso, Stanford University Unstructured (SU2): An open-source integrated computational environment for multi-physics simulation and design, 51st AIAA Aerospace Sciences Meeting including the New Horizons Forum and Aerospace Exposition.

[29] P. Spalart, S. Allmaras, A one-equation turbulence model for aerodynamic flows, in: 30th Aerospace Sciences Meeting and Exhibit, AIAA, Reno, NV, 1992.

[30] F. Fusi, Robust shape optimization of fixed and morphing rotorcraft airfoils, Ph.D. Thesis, Politecnico di Milano (January 2016).

[31] G. Kenway, J. R. R. A. Martins, Multipoint high-fidelity aerostructural optimization of a transport aircraft configuration, Journal of Aircraft 51 (1) (2014) 144–160.

[32] M. Drela, Xfoil: An analysis and design system for low reynolds number airfoils., Conference on Low Reynolds Number Airfoil Aerodynamics, University of Notre Dame 54 (1989) 1–12.

[33] M. B. Giles, M. Drela, Viscous-inviscid analysis of transonic and low reynolds number airfoils, AIAA Journal 25 (10) (1987) 1347–1355.

[34] J. Stack, W. Lindsey, R. Littell, The compressibility burble and the effect of compressibility on pressures and forces acting on an airfoil, Tech. Rep. TR 646, NACA (1939).

[35] G. Zografakis, G. Barakos, Transition modelling for rotorcraft CFD, in: 34th European Rotorcraft Forum, Liverpool, UK, 2008.

[36] G. Wilke, Applying multi-objective variable-fidelity optimization techniques to industrial scale rotors: Blade designs for cleansky, in: Prooceedings of the European Rotorcraft Forum, Munich, Germany, 2015.

[37] R. L. Bielawa, Rotary wing structural dynamics and aeroelasticity, AIAA, 2006, 2nd Edition.

[38] A. Morris, C. Allen, T. Rendall, Aerodynamic optimisation of hovering helicopter rotors using efficient and flexible shape parameterisation, in: 26th AIAA Applied Aerodynamics Conference, 2008.

[39] I. H. Abbott, A. von Doenhoff, Theory of wing section, Dover Publications, Inc., New York, 1949.

[40] B. M. Kulfan, J. E. Bussoletti, "Fundamental" Parametric Geometry Representations for Aircraft Component Shapes, in: 11th AIAA/ISSMO

Multidisciplinary Analysis and Optimization Conference, Portsmouth, VA, 2006.

[41] N. Srinivas, K. Deb, Multiobjective function optimization using non-dominated sorting genetic algorithms, Evolutionary Computation 2 (3) (1994) 221–248.

[42] P. Congedo, C. Corre, J.-M. Martinez, Shape optimization of an airfoil in a BZT flow with multiple-source uncertainties, Computer Methods in Applied Mechanics and Engineering 200 (1-4) (2011) 216–232.

[43] D. S. Lee, J. Periaux, E. Onate, L. F. Gonzalez, N. Qin, Active Transonic Aerofoil Design Optimization Using Robust Multiobjective Evolutionary Algorithms, Journal of Aircraft 48 (3) (2011) 1084–1094.

[44] R. A. E. Mäkinen, J. Periaux, J. Toivanen, Shape design optimization in 2d aerodynamics using genetic algorithms on parallel computers, in: Parallel Computational Fluid Dynamics, Elsevier Science, 1995, pp. 395–402.

[45] D. Xiu, G. E. Karniadakis, The Wiener–Askey Polynomial Chaos for Stochastic Differential Equations, SIAM Journal on Scientific Computing 24 (2) (2002) 619–644.

[46] F. Fusi, P. Congedo, A. Guardone, G. Quaranta, Shape optimization under uncertainty of morphing airfoils, Acta Mechanica (2017) 1–22Article in Press. doi:10.1007/s00707-017-2049-3.

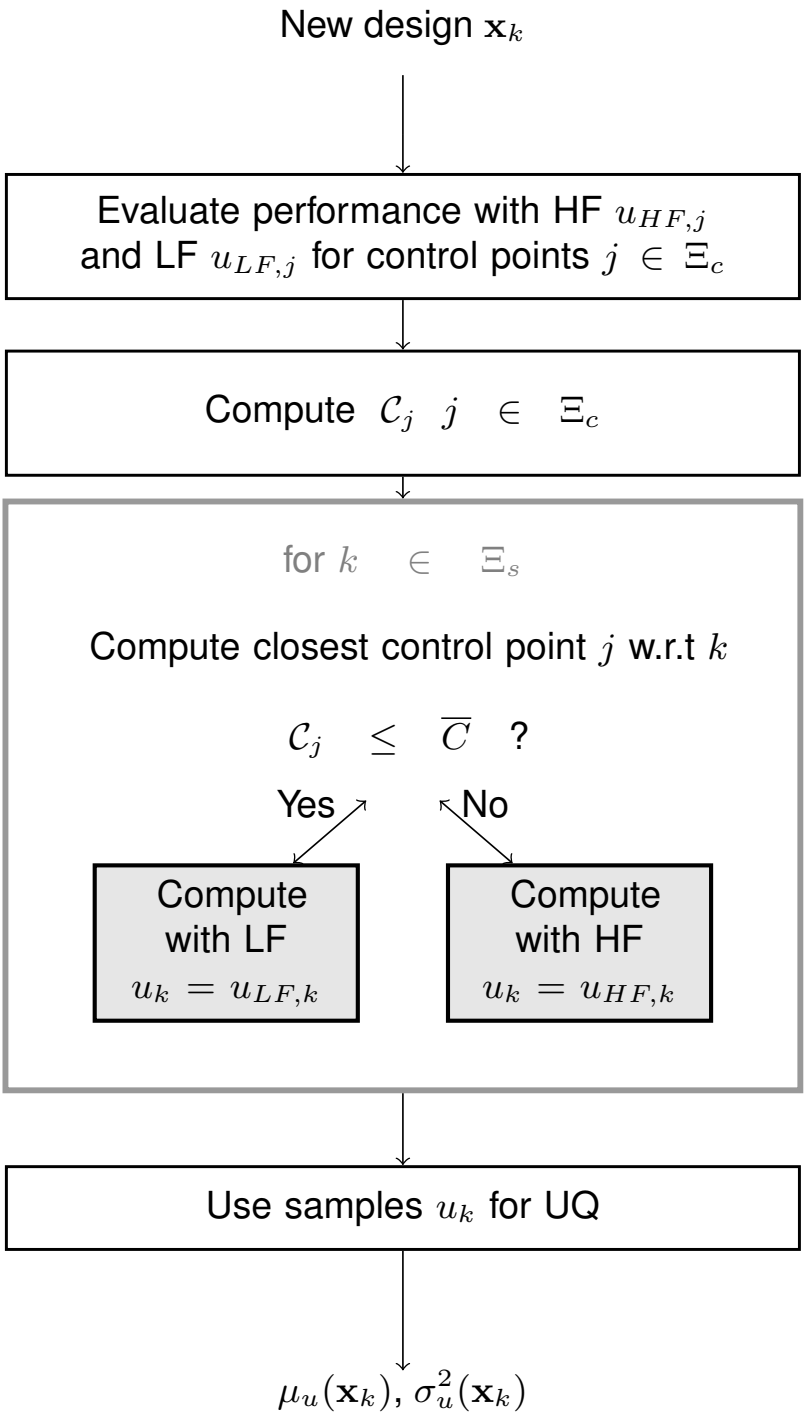




Figure 10: Outer NSGA loop for $\boldsymbol{x}_s$ and inner trim loop to determine $\overline{\alpha}$.

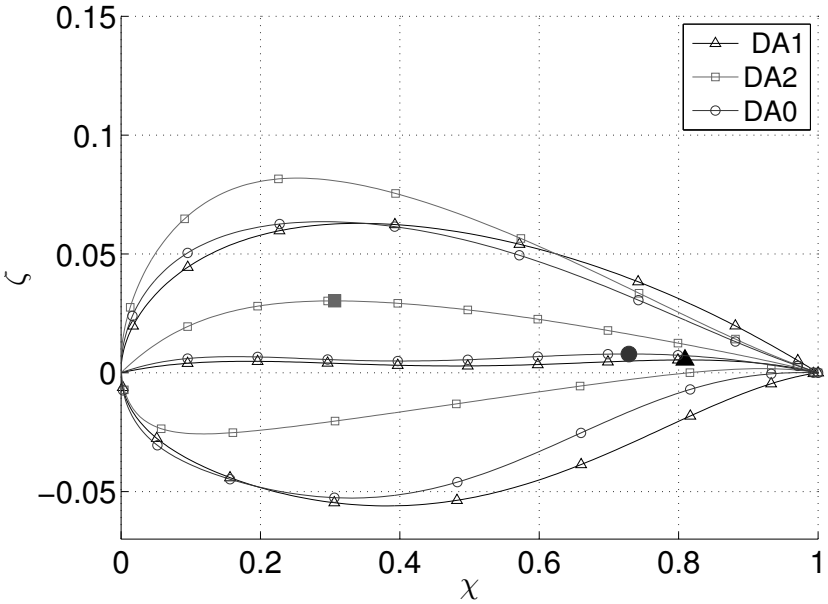


Figure 11: Optimal airfoil geometries for optimization problem DA1, DA2 and DA0.

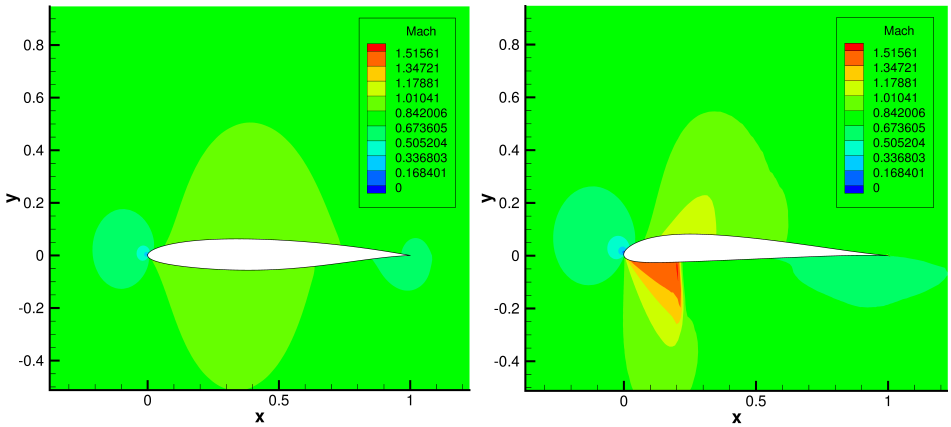


(a) DA1




(b) DA2

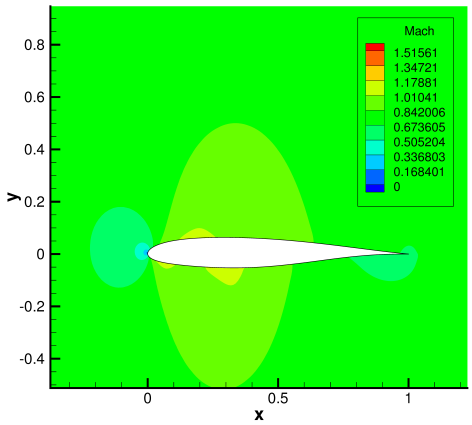


(c) DA0

Figure 12: Mach number contour on the advancing side for airfoil optimal airfoils.

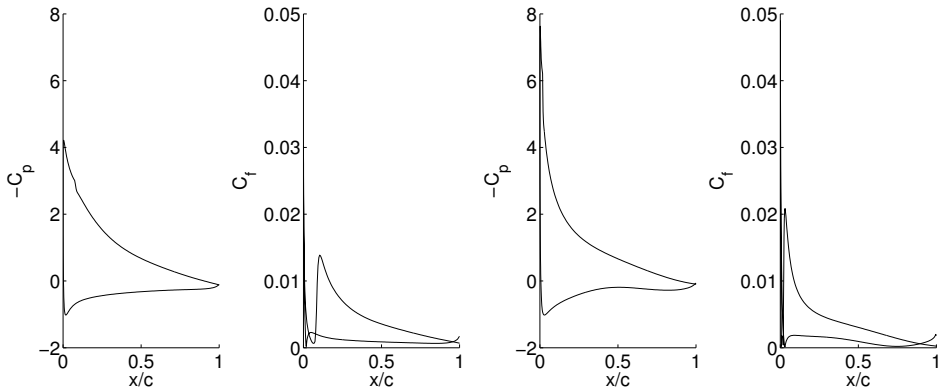


(a) DA2 (b) DA0

Figure 13: Pressure and friction coefficient on the retreating side for optimal airfoil.

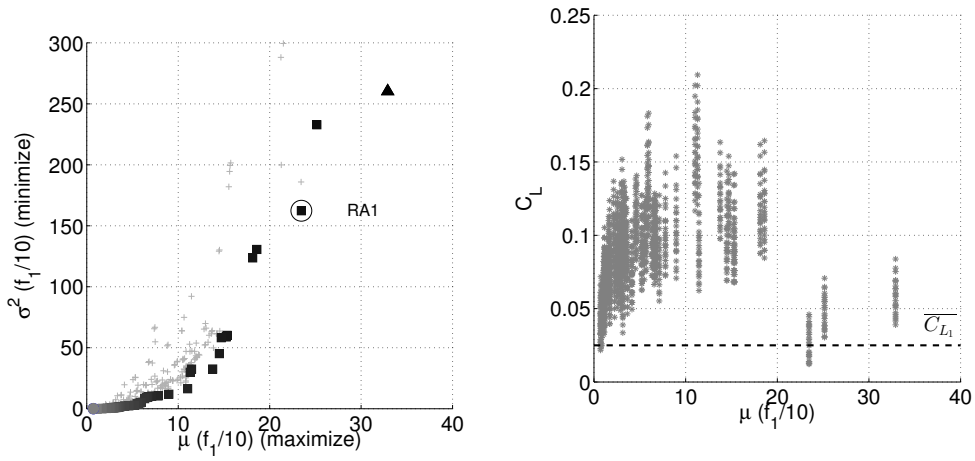


(a) Pareto front. The triangle indicates the airfoil with maximum $\mu$.

(b) Lift coefficient in the samples used in RO1 for the airfoils of the Pareto front.

Figure 14: Results of the robust optimization for the advancing side (RO1).

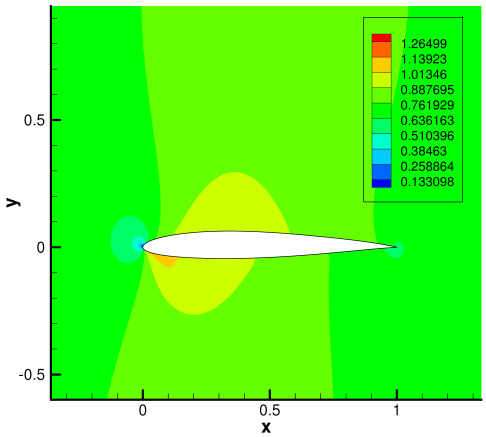


Figure 15: Mach number contour of RA1 airfoil at $\alpha_1|_{\overline{C_{L_1}}} = -1.51$ deg.

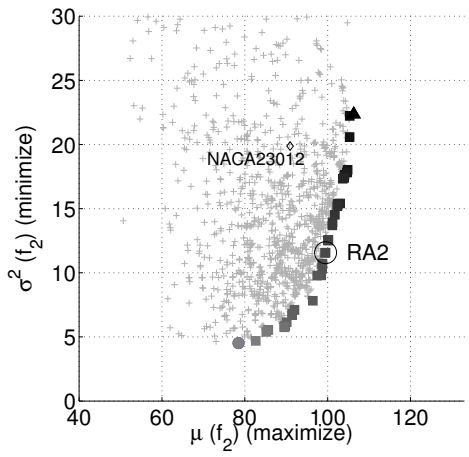


(a) Pareto front.The triangle indicates the airfoil with maximum $\mu$.

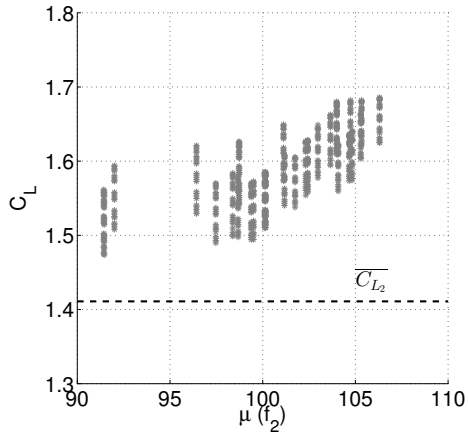


(b) Lift coefficient in the samples used in RO2 for the airfoils of the Pareto front.

Figure 16: Results of the robust optimization for the retreating side (RO2).

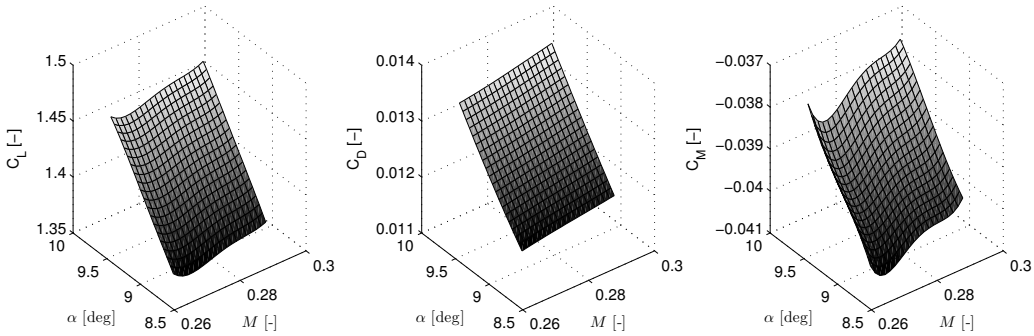


Figure 17: Loads of the DA2 in the uncertainty band around $\alpha_1|_{\overline{C_{L_1}}}$.

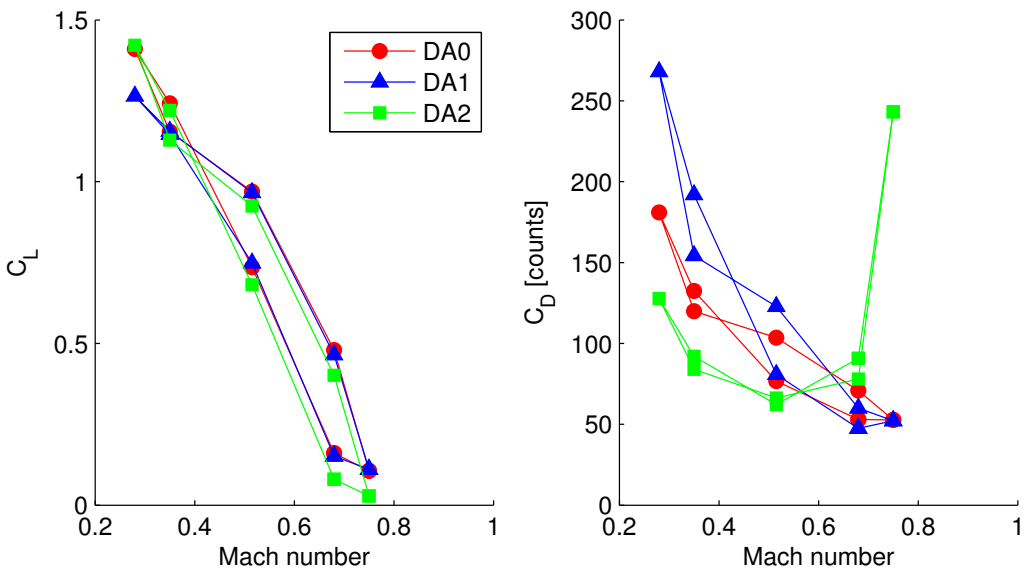


Figure 18: Lift and drag coefficient with azimuth for the deterministic optimal airfoils.

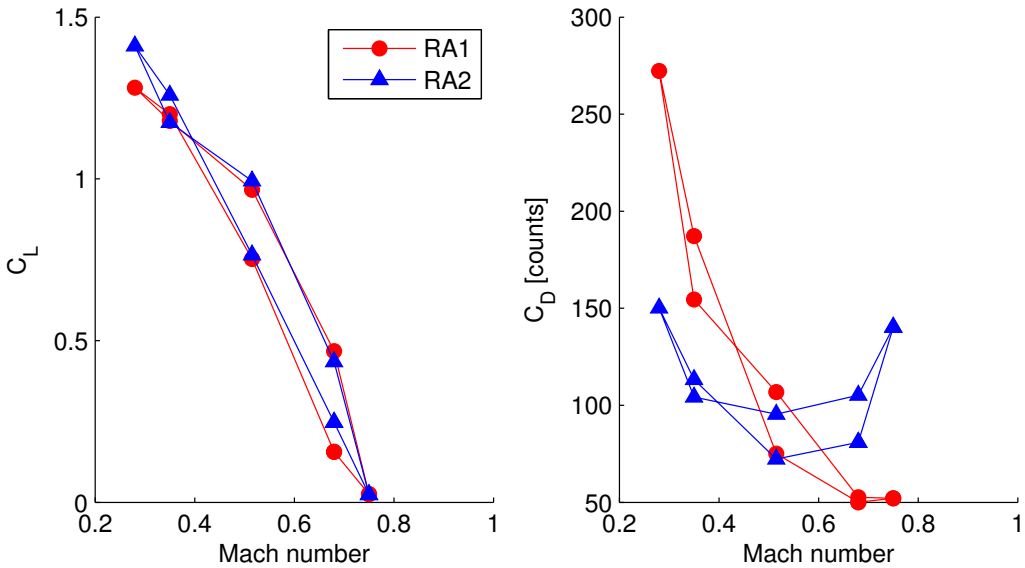


Figure 19: Lift and drag coefficient with azimuth for the robust optimal airfoils.